Computers and Structures 299 (2024) 107343

Contents lists available at ScienceDirect

Computers and Structures

journal homepage: www.elsevier.com/locate/compstruc

Overlapping finite elements for the Navier-Stokes equations

Williams L. Nicomedes [a,*], Klaus-Jürgen Bathe [b], Fernando J. S. Moreira [c], Renato C. Mesquita [a]

[a] Department of Electrical Engineering, Federal University of Minas Gerais, Belo Horizonte, MG 31270-901, Brazil
[b] Department of Mechanical Engineering, Massachusetts Institute of Technology, Cambridge, MA 02139, USA
[c] Department of Electronic Engineering, Federal University of Minas Gerais, Belo Horizonte, MG 31270-901, Brazil

ARTICLE INFO

Keywords:
Overlapping finite elements
Fluid flow
Inf-sup conditions and test
Mixed/hybrid formulations
Navier-Stokes equations

ABSTRACT

The purpose of this paper is to investigate the performance of a certain family of low-order quadrilateral finite elements in the solution of the stationary Navier-Stokes equations governing incompressible fluid flows. These finite elements are derived from the 'overlapping finite elements', first developed for the solution of problems in solid mechanics [5,9,48] and incorporate features of both meshfree and traditional finite element methods. One of their most remarkable properties is the insensitivity to mesh distortions. Also, since the Shepard functions are replaced by a suitable interpolation, the resulting basis functions are entirely polynomial, which allows the numerical integration of the weak forms to be performed with few integration points [6,49]. We also discuss the theoretical reasons for the stability of the solutions, that is, the absence of spurious pressure modes, and show that the proposed discretization scheme passes the relevant inf-sup test.

1. Introduction

The finite element method has a long history of applications in computational fluid dynamical calculations. The large amount of literature devoted to this topic shows the interest in the finite element solution methods [3,17,23,50].

In order to conceive of a numerical method that has the potential to be used in engineering practice, we look for a procedure satisfying four criteria: (1) High predictive capability even in distorted meshes, (2) Low overall solution effort, (3) Ease of imposing Dirichlet boundary conditions, (4) Robustness and reliability, e.g. no dependence on adjustable parameters.

Standard finite element methods (based on either nodal or vector basis functions) do not entirely satisfy criterion (1), because they require a mesh formed of elements with a reasonable degree of quality, i.e., the shape of the triangles and quadrilaterals (or tetrahedra and bricks, prisms) must be as regular as possible. Consequently, a considerable effort must be spent to ensure that mesh generators produce a suitable outcome (elements with either too small or too large internal angles should be avoided) [19,26].

Meshfree (or meshless) methods in principle do not suffer from this issue since they are not based on meshes. However, meshfree methods may employ basis functions which are non-polynomial, like the Meshless Local Petrov-Galerkin (MLPG) [1,41–43], and the Method of Finite Spheres (MFS) [31,35]. Then the process of numerical integration requires many quadrature points, rendering the procedures quite expensive, which means that these methods do not satisfy criterion (2). Other meshfree methods, such as the Smoothed-Particle Hydrodynamics (SPH) and the Element-Free Galerkin (EFG) methods suffer from difficulties in imposing the Dirichlet boundary conditions directly (the latter generally uses moving least squares (MLS) basis functions, which do not satisfy the Kronecker delta property [40]). In this way, they fail to satisfy criterion (3) and the SPH schemes being based on numerical factors also do not satisfy criterion (4).

In discontinuous Galerkin methods, the local approximation spaces within the elements are usually discontinuous across the element interfaces, and the continuity is imposed through an "appropriate" selection of numerical fluxes and stabilization parameters [21,39,47]. In this way, these schemes fail to satisfy criterion (4).

In this work, we present a method that satisfies the four criteria listed above. The method is based on the concept of 'overlapping finite elements', abbreviated as 'OFE', recently introduced for the analysis of problems in solid mechanics [5,9,48]. The OFE method combines desirable features of both finite element and meshfree methods (in particular, the method of finite spheres (MFS), of which it is an evolution [35]). As the traditional FEM, the OFE method also uses polynomial basis functions, which allows the numerical integration to be performed with relatively few quadrature points, and also, as in the traditional

* Corresponding author.
E-mail address: wnicomedes@eng-ele.grad.ufmg.br (W.L. Nicomedes).

https://doi.org/10.1016/j.compstruc.2024.107343
Received 21 January 2024; Accepted 13 March 2024
Available online 25 May 2024

FEM, the Dirichlet boundary conditions are directly imposed. As for meshfree methods, the OFE has a very reduced dependence on the quality of the mesh, hence very distorted elements may be used around complicated geometries, like holes and interfaces, and an 'inexpensively generated mesh' can be used. Since the procedure is not dependent on adjustable factors, it is also robust and reliable and all four criteria are satisfied. The effectiveness of the OFE method has been demonstrated in a number of publications [6,15,27–29,32,36–38,49].

A more comprehensive discussion of the OFE in comparison with other numerical methods is given in the references cited above. We shall focus here on adopting the OFE to the solution of problems in fluid dynamics.

We are interested in the inflow/outflow type of problems, in which the boundary of the domain is divided into two parts: On the first part, Dirichlet conditions are prescribed, which model both the inflow of the fluid into the domain and also the no-slip condition along the walls. On the second part of the boundary, the outflow of the fluid from the domain is imposed. We are thus led to the traditional 2-field mixed formulation of the Navier-Stokes equations, with the pair of unknowns $(\mathbf{u}, p)$ where $\mathbf{u}$ is the velocity field and p is the pressure. The formulation is given in Section 2.

The discretization procedure and the basis functions used in the finite-dimensional representation of $\mathbf{u}$ and p are discussed in Section 3. In Section 4, we consider the inf-sup condition governing the well-posedness of the discrete problems and perform some studies using the inf-sup test concerning the convergence and stability of the solutions using regular and distorted meshes. Based on these studies we identify pairs of interpolations for OFE that are stable and robust, i.e., these OFE satisfy the inf-sup condition without the need for stabilization terms and tunable parameters. Finally we illustrate the use and effectiveness of the proposed OFE in the solutions of some fluid dynamical problems.

2. The problem

2.1. Strong form

We are interested in solving the dimensionless Navier-Stokes equations governing incompressible fluid flows, in a bounded polygonal (Lipschitz) domain $\Omega \subset \mathbb{R}^2$:

Find $(\mathbf{u}, p)$ such that

$$
\begin{aligned}
&-\frac{1}{Re}\nabla^2\mathbf{u} + (\mathbf{u}\cdot\nabla)\mathbf{u} + \nabla p = \mathbf{f}, \quad \text{in } \Omega,\\
&\nabla\cdot\mathbf{u} = 0, \quad \text{in } \Omega,\\
&\mathbf{u} = \mathbf{g}_D, \quad \text{on } \Gamma_D,\\
&\hat{\mathbf{n}}\cdot\bar{\bar{\boldsymbol{\sigma}}} = \mathbf{g}_N, \quad \text{on } \Gamma_N.
\end{aligned}
\tag{2a}
$$

The boundary $\partial\Omega$ is such that $\partial\Omega = \bar{\Gamma}_D \cup \bar{\Gamma}_N$, where Γ_D and Γ_N are open subsets of $\partial\Omega$. We assume that $\Gamma_D \neq \emptyset$ and $\Gamma_N \neq \emptyset$. Moreover, $\Gamma_D \cap \Gamma_N = \emptyset$. In (2a), Re is the Reynolds number, $\mathbf{f}$ is the body force, and $\mathbf{g}_D$ is some known function to be prescribed at the Dirichlet boundary. Also

$$
\bar{\bar{\boldsymbol{\sigma}}} = \frac{1}{Re}\nabla\mathbf{u} - p\bar{\bar{\mathbf{I}}},
$$

and the function $\mathbf{g}_N$ is given. However, in inflow/outflow problems, we usually have $\mathbf{g}_N = \mathbf{0}$. Finally, $\hat{\mathbf{n}}$ is the outward-pointing unit normal vector defined along the boundary $\partial\Omega$, and $\bar{\bar{\mathbf{I}}}$ is the identity tensor.

2.2. Weak form

Let $L^2(\Omega)$ denote the Lebesgue space of all square integrable functions defined on Ω, and let $H^1(\Omega)$ denote the Sobolev space formed by all functions in $L^2(\Omega)$ whose (weak) first derivatives are also in $L^2(\Omega)$. We now introduce the trial space:

$$
\mathbf{X} = \left\{ \mathbf{v} \in \mathbf{H}^1(\Omega) \mid \mathbf{v}|_{\Gamma_D} = \mathbf{g}_D \right\},
\tag{2b}
$$

of all vector functions $\mathbf{v}$ in $\mathbf{H}^1(\Omega) = H^1(\Omega)\times H^1(\Omega)$ whose trace along Γ_D is equal to the given function $\mathbf{g}_D$. The space of functions used for testing is $\mathbf{H}^1_{0,\Gamma_D}(\Omega) = H^1_{0,\Gamma_D}(\Omega)\times H^1_{0,\Gamma_D}(\Omega)$, in which $H^1_{0,\Gamma_D}(\Omega)$ denotes the set of all functions in $H^1(\Omega)$ whose trace along Γ_D is equal to zero [14]. Assuming that the velocity field $\mathbf{u}$ belongs to $\mathbf{X}$, that the pressure field p belongs to $L^2(\Omega)$, and that the body force $\mathbf{f}$ belongs to $\mathbf{L}^2(\Omega) = L^2(\Omega)\times L^2(\Omega)$, we can use Green's identities to show that the weak form of problem (2a) is:

Find $(\mathbf{u}, p) \in \mathbf{X}\times L^2(\Omega)$ such that

$$
\begin{aligned}
&\int_\Omega \frac{1}{Re}\nabla\mathbf{u} : \nabla\mathbf{v}\,d\Omega + \int_\Omega (\mathbf{u}\cdot\nabla\mathbf{u})\cdot\mathbf{v}\,d\Omega - \int_\Omega p\nabla\cdot\mathbf{v}\,d\Omega\\
&-\oint_{\partial\Omega}(\hat{\mathbf{n}}\cdot\bar{\bar{\boldsymbol{\sigma}}})\cdot\mathbf{v}\,d\Gamma = \int_\Omega \mathbf{f}\cdot\mathbf{v}\,d\Omega, \ \text{for any } \mathbf{v}\in\mathbf{H}^1_{0,\Gamma_D}(\Omega),\\
&\int_\Omega q\,\nabla\cdot\mathbf{u}\,d\Omega = 0, \ \text{for any } q\in L^2(\Omega),
\end{aligned}
\tag{2c}
$$

where $\mathbf{u}|_{\Gamma_D} = \mathbf{g}_D$. We note that the second equation in (2a) – the *incompressibility condition* – is imposed weakly in (2c). Note also that the boundary integral in (2c) is zero due to the choices of $\mathbf{g}_N$ and $\mathbf{v}$.

2.3. Finite dimensional case

We introduce generic finite-dimensional (or 'discrete') subspaces $\mathbf{X}_h \subset \mathbf{X}$ in (2b) and $Y_h \subset L^2(\Omega)$. The finite-dimensional counterpart to problem (2c) is given by:

Find $(\mathbf{u}_h, p_h) \in \mathbf{X}_h \times Y_h$ such that

$$
\begin{aligned}
&\int_\Omega \frac{1}{Re}\nabla\mathbf{u}_h : \nabla\mathbf{v}_h d\Omega + \int_\Omega (\mathbf{u}_h\cdot\nabla\mathbf{u}_h)\cdot\mathbf{v}_h d\Omega - \int_\Omega p_h\nabla\cdot\mathbf{v}_h d\Omega\\
&= \int_\Omega \mathbf{f}\cdot\mathbf{v}_h d\Omega, \ \text{for any } \mathbf{v}_h\in\mathbf{X}^0_h,\\
&\int_\Omega q_h\,\nabla\cdot\mathbf{u}_h\,d\Omega = 0, \ \text{for any } q_h\in Y_h.
\end{aligned}
\tag{2d}
$$

The Dirichlet boundary conditions are easily imposed by simply fixing the value of some coefficients (degrees of freedom, or DoF's) on Γ_D, which means that the linear subspace $\mathbf{X}^0_h$ is constructed from $\mathbf{X}_h$ simply by making the DoF's along Γ_D equal to zero, so that $\mathbf{X}^0_h \subset \mathbf{H}^1_{0,\Gamma_D}(\Omega)$. The solution of the nonlinear problem (2d) can be obtained using a number of different solution schemes, like Newton-Raphson iterations and variations thereof, and Picard iterations, see e.g [3]. In each case, the important point is that the solution needs to be obtained to sufficient accuracy. The discretized fields can be expanded as $\mathbf{u}_h = \bar{\mathbf{H}}_\mathbf{u}\widetilde{\mathbf{U}}$ and $p_h = \bar{\mathbf{H}}_p\widetilde{\mathbf{P}}$, where $\bar{\mathbf{H}}_\mathbf{u}$ and $\bar{\mathbf{H}}_p$ are suitable matrices collecting the velocity and pressure basis functions, respectively, and $\widetilde{\mathbf{U}}$ and $\widetilde{\mathbf{P}}$ are vectors collecting the DoF's. The testing functions are expanded likewise. Substitution into (2d), together with a treatment for the nonlinearity (see above), allows us to obtain the system of linear algebraic equations which yields the next solution vectors ($\widetilde{\mathbf{U}}^{n+1}$ and $\widetilde{\mathbf{P}}^{n+1}$) in terms of the previous solution vectors ($\widetilde{\mathbf{U}}^{n}$ and $\widetilde{\mathbf{P}}^{n}$). Assuming that this iterative procedure calculates the DoF vectors $\widetilde{\mathbf{U}}^{n}$ and $\widetilde{\mathbf{P}}^{n}$ for $n = 1, 2, 3, \cdots$, we then assemble (i.e., concatenate) the solution vectors $\widetilde{\mathbf{U}}^{n}$ and $\widetilde{\mathbf{P}}^{n}$ into the solution vector $\widetilde{\mathbf{W}}^{n}$, thus forming a sequence $\left(\widetilde{\mathbf{W}}^{1}, \widetilde{\mathbf{W}}^{2}, \widetilde{\mathbf{W}}^{3}, \cdots\right)$. The relative error is given as $\varepsilon_n = \|\widetilde{\mathbf{W}}^{n+1} - \widetilde{\mathbf{W}}^{n}\|/\|\widetilde{\mathbf{W}}^{n}\|$, where $\|\cdot\|$ is the Euclidean norm of a vector. The iteration is continued until convergence is reached to a reasonable tolerance, in our solutions given until $\varepsilon_n < 10^{-6}$.

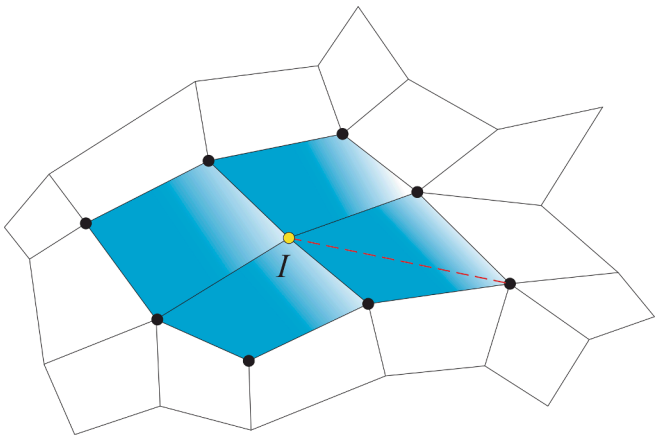

Fig. 1. A portion of some arbitrary partition $\mathscr{C}_h$. The four cells indicated in blue contain node I as a vertex. The nodes in the support set $\mathscr{N}_I$ are given by the union of the nodes in these four blue cells, and are indicated by black dots (in addition to node I itself). The largest distance between node I and the nodes in $\mathscr{N}_I$ is indicated by a dashed red line. All nodes in the partition have their associated support sets, see [27]. (For interpretation of the references to colour in this figure legend, the reader is referred to the web version of this article.)

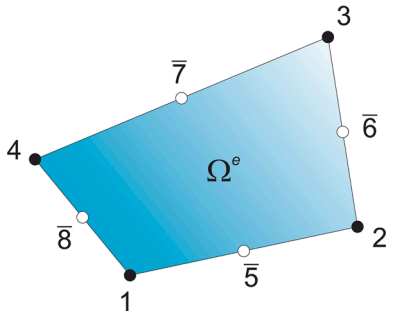

Fig. 2. A cell Ω^e, indexed by the number 'e'. The nodes at the four vertices are indicated by the (local) indices 1, 2, 3, and 4. The DoF's (coefficients $\widetilde{s}_{I,m}$ in the expansion (3b)) are assigned to these nodes only. The points $\bar{5}$, $\bar{6}$, $\bar{7}$, and $\bar{8}$ are located at the midpoints of the edges; there are no DoF's assigned to them, since they are used just as an aid to construct the serendipity shape functions $\widehat{h}_{JI}$ in (3e), see [36].

Table 1
Nomenclature of OFE spaces.

Space	Local bases
OFE_0	$\{1\}$,
OFE_1	$\{1, X_I, Y_I\}$,
OFE_2	$\{1, X_I, Y_I, X_I^2, X_I Y_I, Y_I^2\}$.

We will not investigate the existence and uniqueness of the velocity field $\mathbf{u}_h$ in (2d) since this condition is surely satisfied in our solution, but will instead investigate whether a unique solution of the pressure field is guaranteed. That is, if the discrete problem (2d) admits some solution pair $(\mathbf{u}_h, p_h)$, there could in principle exist another solution pair with the same velocity field $\mathbf{u}_h$ and a different pressure field r_h. This possibility is ruled out iff the following *inf-sup condition* is satisfied:

There is some constant $\beta_h > 0$ such that

$$\inf_{q_h \in Y_h \setminus \{0\}} \sup_{\mathbf{v}_h \in \mathbf{X}_h^0 \setminus \{0\}} \frac{\int_\Omega q_h \nabla \cdot \mathbf{v}_h d\Omega}{\|q_h\|_{L^2(\Omega)} \|\mathbf{v}_h\|_{\mathbf{H}^1(\Omega)}} \geq \beta_h, \tag{2e}$$

where $\|\cdot\|_{L^2(\Omega)}$ and $\|\cdot\|_{\mathbf{H}^1(\Omega)}$ denote the norms in $L^2(\Omega)$ and $\mathbf{H}^1(\Omega)$,

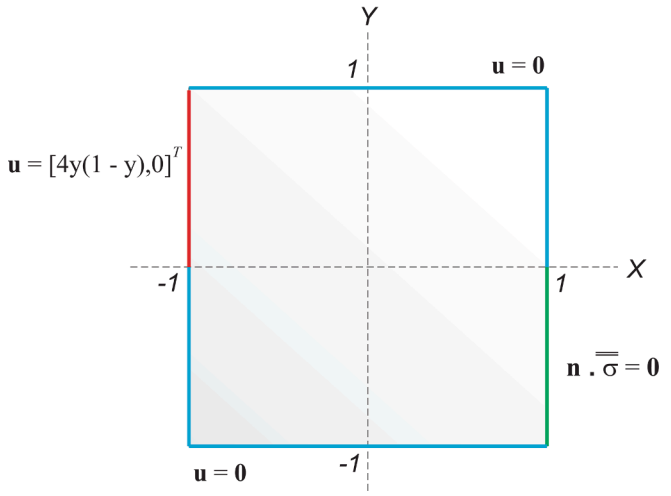

Fig. 3. Geometry (dimensionless units) and boundary conditions relative to the problem from Section 4. The inlet and the outlet are shown in red and green, respectively, whereas the no-slip walls are shown in blue. (For interpretation of the references to colour in this figure legend, the reader is referred to the web version of this article.)

respectively. Hence if (2e) is satisfied spurious pressure modes will not be present [3]. The discrete inf-sup condition (2e) has to be proven for each particular choice of $\mathbf{X}_h$ and Y_h. For some pairs of traditional finite elements, the inf-sup condition (2e) can be analytically proven to hold [3,20,22]. However, these proofs are difficult to obtain, and a proof may be out of reach for a given pair of spaces $\mathbf{X}_h$ and Y_h, as for the case using the OFE basis functions. Hence we shall use a numerical test, known as the Chapelle-Bathe test or *inf-sup test* presented in [16]. This test is not an analytical proof that the inf-sup condition is satisfied for a specific pair of $\mathbf{X}_h$ and Y_h, but we judiciously use that *if the inf-sup test is not passed, the inf-sup condition is not satisfied*. Since the publication of the test, it has been successfully applied to a multitude of problems, in both classical finite element [4,11,12,33] and meshfree analyses [18,45,46].

3. Finite-dimensional function spaces for overlapping finite elements

3.1. OFE subspaces

Let us consider a finite-dimensional space for approximating a generic scalar function s_h defined on Ω using the quadrilateral OFE proposed in [36]. Suppose that a total of N nodes have been scattered throughout Ω and along its boundary $\partial\Omega$. Let $\mathscr{C}_h$ denote a partition of the computational domain Ω into quadrilateral cells, so that

$$\bar{\Omega} = \bigcup_e \bar{\Omega}^e,$$

where the index 'e' runs from 1 to the total number of cells in $\mathscr{C}_h$, and where Ω^e is the interior of the cell indexed by 'e'. For each node $I = 1, \cdots, N$, its location within $\bar{\Omega}$ is denoted by $\mathbf{x}_I = (x_I, y_I)$. The *support set* $\mathscr{N}_I$ is given by the union of the nodes of all cells e in $\mathscr{C}_h$ that contain node I as a vertex, see Fig. 1. Let r_I be the maximum distance between $\mathbf{x}_I$ and the nodes in $\mathscr{N}_I$, i.e.,

$$r_I = \max_{J \in \mathscr{N}_I} \|\mathbf{x}_I - \mathbf{x}_J\|, \tag{3a}$$

see Fig. 1. As in the method of finite spheres [25,31,35,44–46], each node $I = 1, \cdots, N$ carries a set of linearly-independent local basis functions $\{l_{I,1}, l_{I,2}, \cdots\}$, together with a set of coefficients (or DoF's) $\{\widetilde{s}_{I,1}, \widetilde{s}_{I,2} \cdots, \}$ so that we obtain a linear combination:

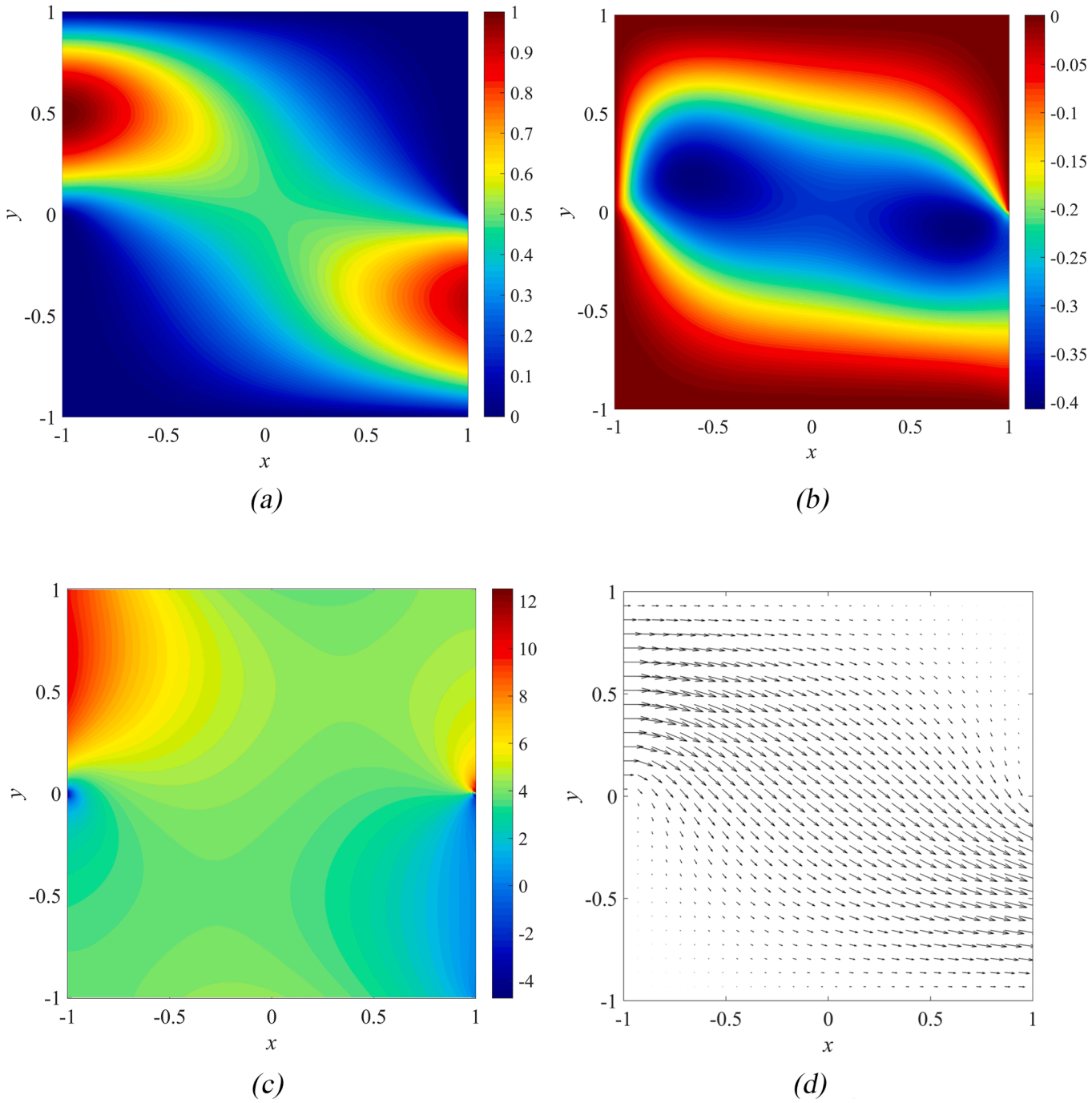

Fig. 4. The finite element reference solution $(\mathbf{u}_{Ref}, p_{Ref})$, provided by the traditional $\boldsymbol{Q}_2/Q_1$ pair, using a uniform mesh with 128×128 square elements. *(a)* Horizontal component of the velocity field. *(b)* Vertical component of the velocity field. *(c)* The pressure field. *(d)* Arrows indicating the direction of the velocity field.

$$S_I = l_{I,1}\widetilde{s}_{I,1} + l_{I,2}\widetilde{s}_{I,2} + \cdots = \sum_m l_{I,m}\widetilde{s}_{I,m}, \tag{3b}$$

associated with each node $I = 1, \cdots, N$, and defined for any point $\mathbf{x} = (x, y)$ within $\bar{\Omega}$. The coefficients $\widetilde{s}_{I,1}, \widetilde{s}_{I,2} \cdots$, are the DoF's in the expansion of s_h. In the OFE approximations, we use monomials in the local bases as:

$$S_I = 1 \cdot \widetilde{s}_{I,1} + X_I\widetilde{s}_{I,2} + Y_I\widetilde{s}_{I,3} + \cdots, \tag{3c}$$

where $X_I = (x - x_I)/\delta_I$, $Y_I = (y - y_I)/\delta_I$, and $\delta_I = r_I/2$ [36]. We always use $l_{I,1} \equiv 1$, i.e., the first local basis function $l_{I,1}$ is identical to the unity. Given a cell e in $\mathscr{C}_h$, suppose its four 'physical' nodes (each node is originally given a *global* index between 1 and N) are now numbered simply as $1, 2, 3$, and 4 (i.e., we use a *local* numbering), see Fig. 2. The points marked with an overbar $\bar{5}, \bar{6}, \bar{7}$, and $\bar{8}$ are not physical nodes, but indicate the midpoints of the edges of the cell e. At any point $\mathbf{x} = (x, y)$ within Ω^e, our generic scalar function s_h is approximated as:

$$s_h = \sum_{I=1}^{4} \rho_I S_I = \sum_{I=1}^{4} \sum_m \rho_I l_{I,m}\widetilde{s}_{I,m}, \tag{3d}$$

where the S_I are those in (3b). The 'modulating' functions ρ_I are given by:

$$\rho_I = h_I + \beta \sum_J (h_J - h_I)\widehat{h}_{JI}, \tag{3e}$$

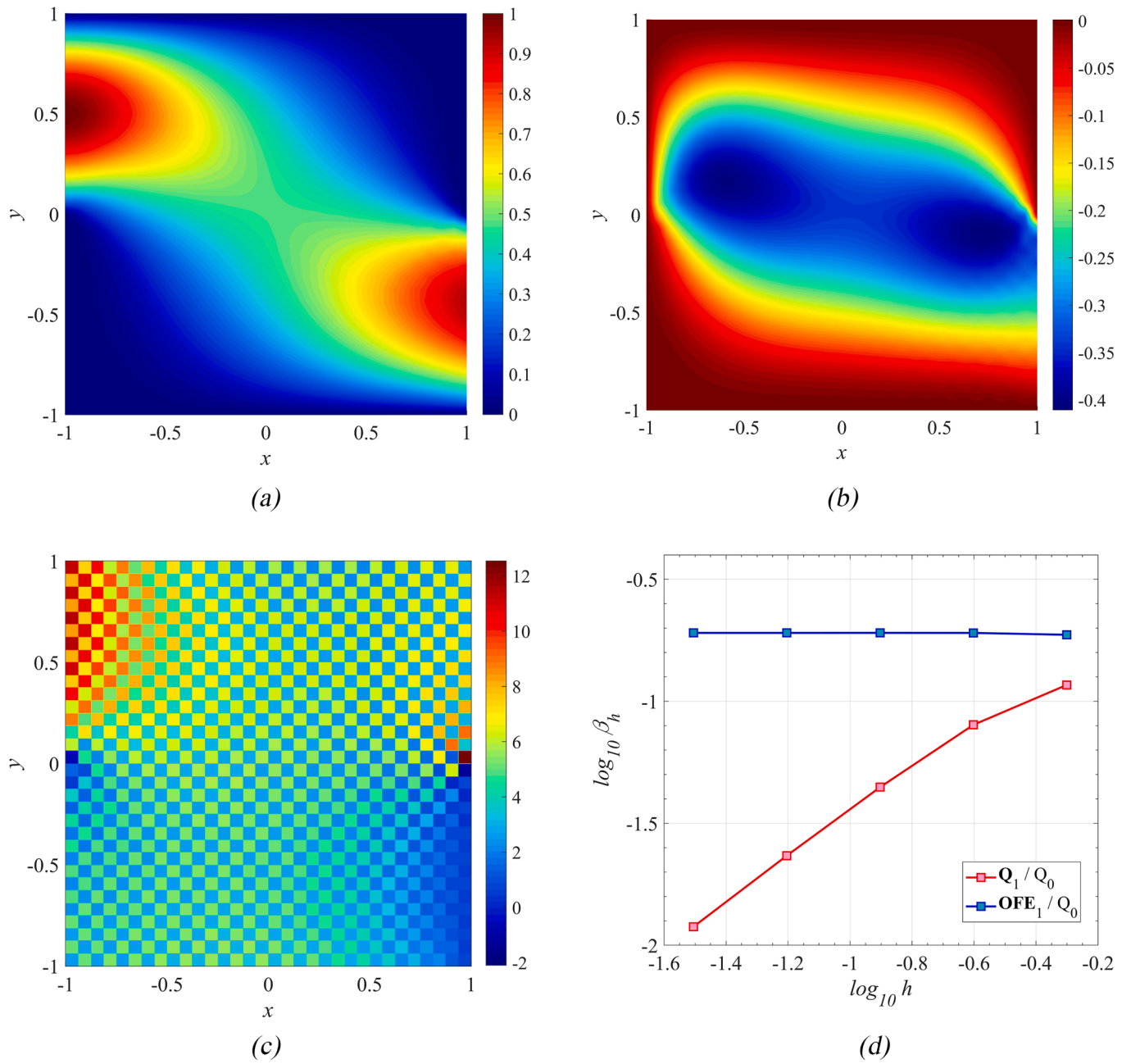

Fig. 5. Finite element solution, calculated using the traditional $\boldsymbol{Q}_1/Q_0$ pair, on a uniform mesh formed by 32×32 square elements. *(a)* Horizontal component of the velocity field. *(b)* Vertical component of the velocity field. *(c)* The pressure field, contaminated by the checkerboard pattern. *(d)* The inf-sup curves calculated in a sequence of uniform meshes of $N \times N$ elements each. For the $\boldsymbol{Q}_1/Q_0$ pair, the inf-sup constants β_h present a steady decay as h becomes smaller. This behavior is in stark contrast with that regarding the $\mathbf{OFE}_1/Q_0$ pair, for which the inf-sup constants attain a 'plateau'.

for $I = 1,\cdots,4$, where $\beta = 0.01$ see [36]. The function h_I is the traditional 4-node bilinear shape function associated with node I, and the index J runs over the two nodes directly connected to node I. Finally, $\widehat{h}_{JI}$ is the traditional 8-node serendipity shape function associated with the midpoint between nodes J and I [3]. For example, $\rho_1 = h_1 + \beta(h_2 - h_1)\widehat{h}_{\bar{5}} + \beta(h_4 - h_1)\widehat{h}_{\bar{8}}$, since nodes 2 and 4 are directly connected to node 1, whereas $\bar{5}$ and $\bar{8}$ are the midpoints between nodes 2 and 1, and between nodes 4 and 1, respectively, see Fig. 2. Considering (3d), it is seen that the interpolations give continuity across the edges of $\mathscr{E}_h$, i.e., $s_h \in C(\bar{\Omega})$.

Since the monomials X_I and Y_I vanish at node I (see (3c)), we also see that $s_h(\mathbf{x}_I) = \widetilde{s}_{I,1}$, for $I = 1,\cdots,N$. The imposition of essential boundary conditions is thus simple: we simply set the first DoF at each node along Γ_D to be equal to the prescribed condition calculated at $\mathbf{x}_I$, and set the other DoF's equal to zero. The result is that the essential boundary conditions are enforced as in the traditional FEM.

3.2. OFE subspaces for the velocity and pressure fields

In this paper, the approximation of scalar quantities (components of the velocity field and the pressure) will be based on sets of constant (degree 0), linear (degree 1), and quadratic (degree 2) monomials in the local bases $\{l_{I,1}, l_{I,2}, \cdots\}$ associated with each node I, see (3c). The resulting spaces are listed in Table 1.

All N nodes in the mesh use local bases with the same number of monomials, so approximations based on the spaces OFE_0, OFE_1, and OFE_2 yield a total of N, $3N$, and $6N$ coefficients (DoF's), respectively, all

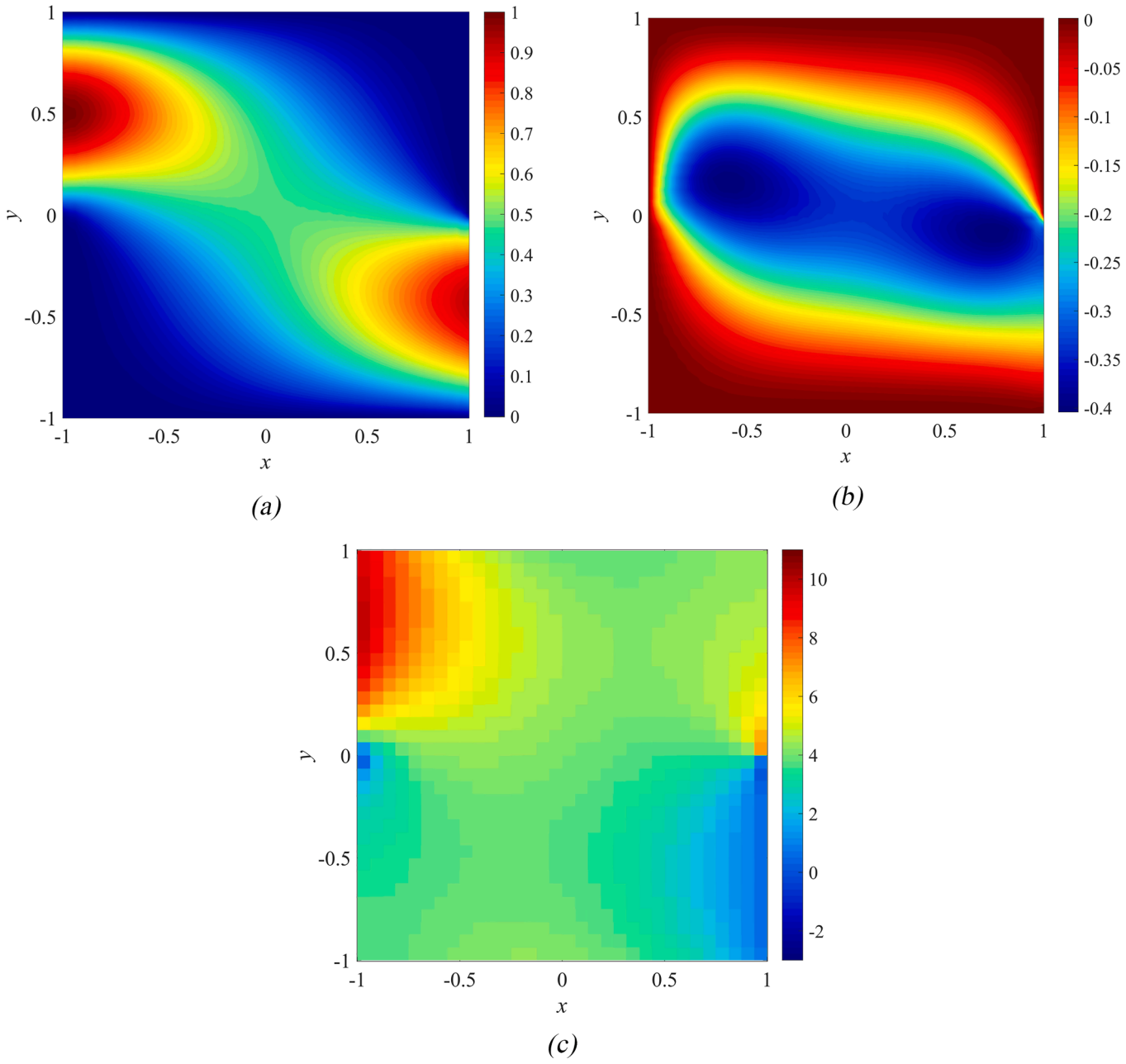

Fig. 6. Finite element solution, calculated using the $\mathbf{OFE}_1/Q_0$ pair, on a uniform mesh formed by 32×32 square elements. *(a)* Horizontal component of the velocity field. *(b)* Vertical component of the velocity field. *(c)* The pressure field, this time not contaminated by the checkerboard pattern.

to be calculated using sparse matrices, as in the standard FEM. The subscript '1' in OFE_1 indicates that each node carries a full degree 1 polynomial, and likewise for the other cases. From now on, the word 'element' will be used to denote a cell together with an interpolation, so that different choices for the interpolations yield different elements. In this paper, the components of the discrete velocity field $\mathbf{u}_h = (u_{h,1}, u_{h,2})$ are calculated within the OFE_1 space; we call the resulting space $\mathbf{OFE}_1 = \text{OFE}_1 \times \text{OFE}_1$ (bold letters denoting a vector quantity), which uses $3N$ DoF's per component (and thus a total of $6N$ DoF's in the calculation of vector $\mathbf{u}_h$). We shall make a brief mention to the space $\mathbf{OFE}_2 = \text{OFE}_2 \times \text{OFE}_2$, which uses $6N$ DoF's per component (and thus $12N$ DoF's in the calculation of $\mathbf{u}_h$). The discrete pressure field p_h is calculated within the OFE_0 space. The OFE spaces just mentioned yield continuous approximations. However, we shall also employ a discontinuous approximation for the pressure field in which p_h is given by the traditional piecewise constant functions [3]. This space will be denoted as Q_0, and the number of DoF's is of course equal to the number of elements in the partition $\mathscr{C}_h$.

3.3. Geometrical modeling and numerical integration

Consider the biunit square $\omega = \{(\xi,\eta) \mid -1 \le \xi \le 1 \text{ and } -1 \le \eta \le 1\}$. In this paper, the geometry of the cell Ω^e in Fig. 2 is described by the following transformation, which takes a point (ξ,η) in ω and returns a point (x,y) in Ω^e:

$$\begin{bmatrix} x \\ y \end{bmatrix} = \sum_{I=1}^{4} h_I(\xi,\eta) \begin{bmatrix} x_I^e \\ y_I^e \end{bmatrix},$$

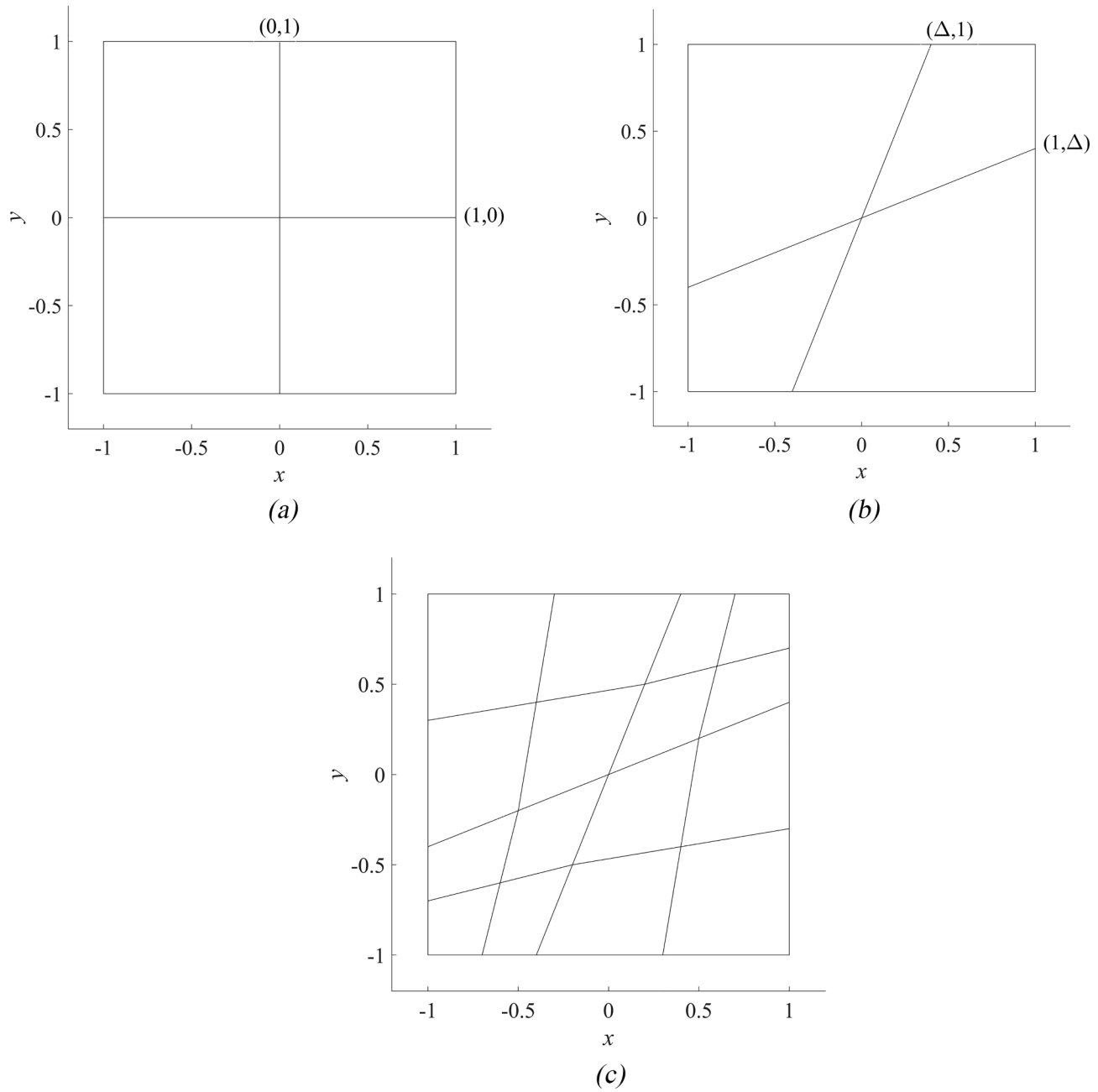

Fig. 7. *(a)* The original square domain Ω, whose sides are equally divided into $N = 2$ equal segments. *(b)* In order to introduce distortion, the middle horizontal segment is tilted upwards, whereas the middle vertical segment is tilted to the right. In this figure, the mesh distortion parameter is given by $\Delta = 0.4$. *(c)* Each cell in *(b)* is subdivided into four other cells.

where (x_I^e, y_I^e), $I = 1, \cdots, 4$ are the 'physical' coordinates of the I-th node (vertex) in Ω^e (assuming a local numbering scheme, as in Fig. 2), and the h_I are the bilinear basis functions defined on ω. When treating the weak forms, the integral of any quantity g over the 'physical' cell Ω^e can be evaluated as:

$$\int_{\Omega^e} g(x,y)d\Omega = \int_{-1}^{1}\int_{-1}^{1} g(x(\xi,\eta), y(\xi,\eta))|\det \boldsymbol{J}^e| d\xi d\eta,$$

where $\det \boldsymbol{J}^e$ is the determinant of the Jacobian matrix associated with the tranformation given above. The derivatives in g with respect to the 'physical' coordinates x and y must be expressed in terms of the derivatives with respect to ξ and η through judicious use of the chain rule, as in standard finite element calculations. If the velocity field is approximated within the space $\mathbf{OFE}_1$, the integral above is evaluated using a 3-point Gaussian quadrature rule along ξ and along η, resulting in 9 integration points per element. On the other hand, if the approximation is made within the space $\mathbf{OFE}_2$, we use a 5 x 5 rule [36]. We are thus led to a very efficient integration process, in stark contrast with the majority of meshfree methods [40], for which the integration process requires a large number of points, when the basis functions are rational expressions.

3.4. Inf-sup testing

Using the discretization procedure, the terms in (2e) can be expressed in matrix form as:

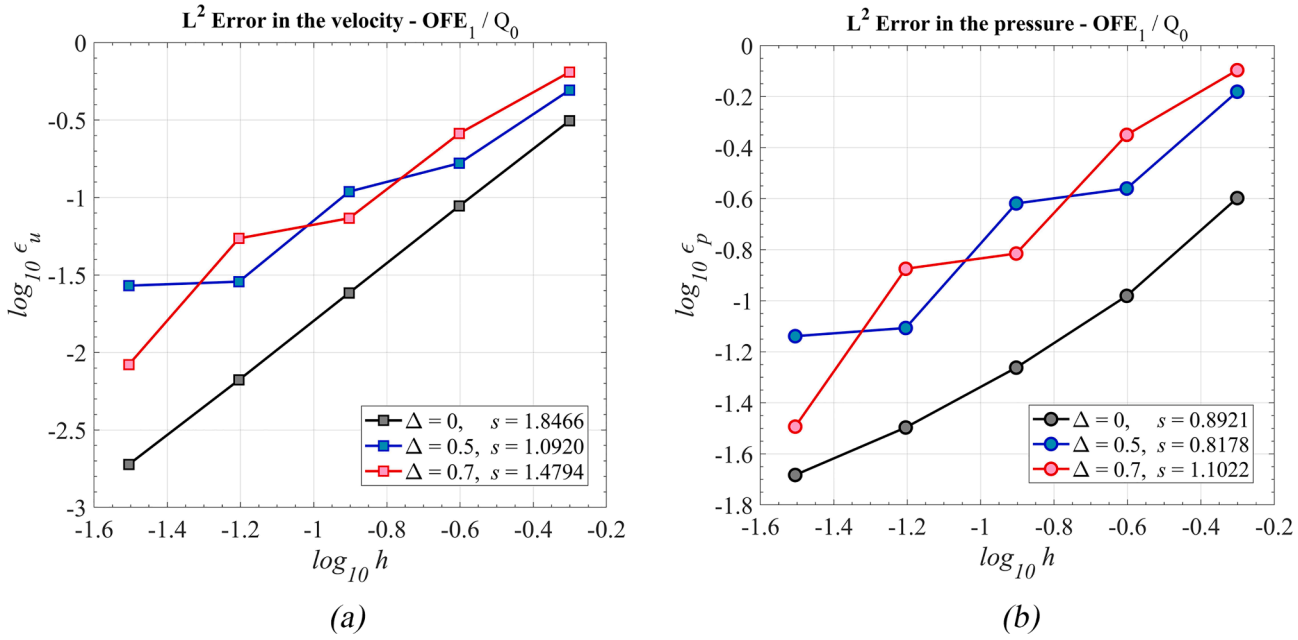

Fig. 8. Convergence curves for the $\mathbf{OFE}_1/Q_0$ pair. The errors are calculated with respect to the $\boldsymbol{Q}_2/Q_1$ reference solution from Fig. 4, using (4c). *(a)* Error in the velocity. *(b)* Error in the pressure. The approximate slopes s are taken from Table 2, and Δ is the mesh distortion parameter.

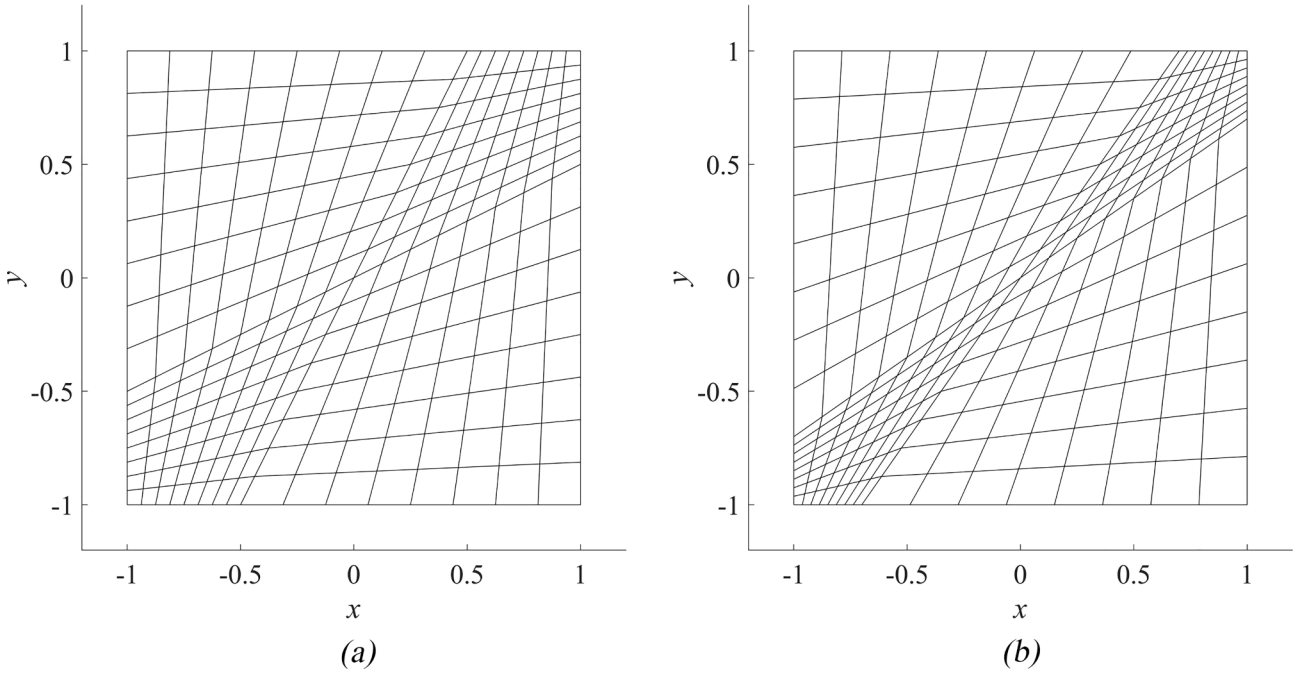

Fig. 9. Examples of distorted meshes, for which $N = 16$. *(a)* Distortion parameter $\Delta = 0.5$. *(b)* Distortion parameter $\Delta = 0.7$.

Table 2
Relative errors for the $\mathbf{OFE}_1/Q_0$ pair.

$\Delta = 0$	$\Delta = 0.5$	$\Delta = 0.7$
$\varepsilon_{\mathbf{u}}(h) \simeq C_1 h^{1.8466}$	$\varepsilon_{\mathbf{u}}(h) \simeq C_2 h^{1.0920}$	$\varepsilon_{\mathbf{u}}(h) \simeq C_3 h^{1.4794}$
$\varepsilon_p(h) \simeq C_4 h^{0.8921}$	$\varepsilon_p(h) \simeq C_5 h^{0.8178}$	$\varepsilon_p(h) \simeq C_6 h^{1.1022}$

$$\int_\Omega q_h \nabla \cdot \mathbf{v}_h \, d\Omega = \widetilde{\mathbf{Q}}^T \, \bar{\mathbb{B}} \, \widetilde{\mathbf{V}},$$

$$\|\mathbf{v}_h\|^2_{\mathbf{H}^1(\Omega)} = \int_\Omega (\mathbf{v}_h \cdot \mathbf{v}_h + \nabla \mathbf{v}_h \, : \nabla \mathbf{v}_h) d\Omega = \widetilde{\mathbf{V}}^T \, \bar{\mathbb{K}} \, \widetilde{\mathbf{V}}, \tag{3f}$$

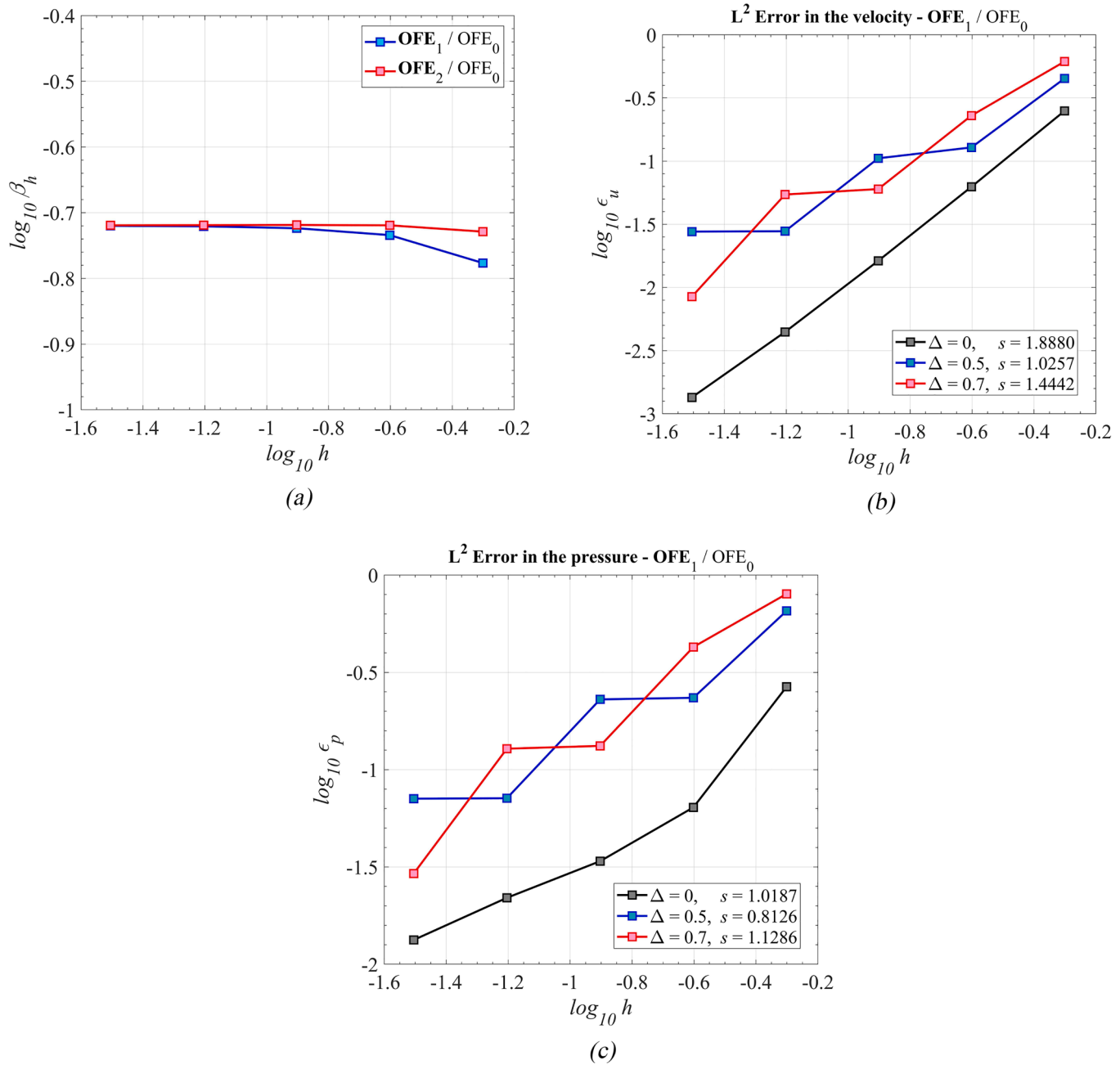

Fig. 10. *(a)* The inf-sup curves calculated in a sequence of uniform meshes with $N \times N$ square elements each. Results concerning the $\mathbf{OFE}_1/\mathrm{OFE}_0$ and $\mathbf{OFE}_2/\mathrm{OFE}_0$ pairs, see Sections 4.2 and 4.3, respectively. For both cases, the inf-sup constants stabilize at a positive value and do not decay as h decreases. *(b)* Convergence curves for the velocity, using the $\mathbf{OFE}_1/\mathrm{OFE}_0$ pair. The errors are calculated with respect to the Q_2/Q_1 reference solution from Fig. 4, using (4c) . *(c)* Convergence curves for the pressure. The approximate slopes s are taken from Table 3, and Δ is the mesh distortion parameter.

$$\|q_h\|^2_{L^2(\Omega)} = \int_\Omega |q_h|^2 d\Omega = \widetilde{\mathbf{Q}}^T \, \bar{\mathbb{Y}} \, \widetilde{\mathbf{Q}}.$$

The vectors $\widetilde{\mathbf{V}}$ and $\widetilde{\mathbf{Q}}$ collect the DoF's in the expansions of $\mathbf{v}_h$ and q_h, respectively. These vectors are pre- and post-multiplied by suitable matrices $\bar{\mathbb{B}}$, $\bar{\mathbb{K}}$, and $\bar{\mathbb{Y}}$. We point out that, because the velocity field $\mathbf{v}_h$ belongs to $\mathbf{X}_h^0$, i.e., $\mathbf{v}_h$ has zero trace along the Dirichlet boundary Γ_D, the DoF's associated with nodes located along Γ_D (and at its endpoints) must effectively be removed from the expansion of $\mathbf{v}_h$ (because they are constrained to be zero), and consequently the corresponding rows and columns must be removed from matrices $\bar{\mathbb{B}}$ and $\bar{\mathbb{K}}$. For example, if the discrete velocity field $\mathbf{v}_h = (v_{h,1}, v_{h,2})$ is calculated within the space $\mathbf{OFE}_1$, we saw in Section 3.2 that the components $v_{h,1}$ and $v_{h,2}$ require 3 DoF's per node. Suppose there are N_D nodes located along Γ_D (plus the endpoints). All three DoF's associated with each of these nodes must be set to zero, so that the complete specification of $v_{h,1}$ now requires $3(N - N_D)$ DoF's, and likewise for $v_{h,2}$. In this way the complete vector $\widetilde{\mathbf{V}}$ collecting all DoF's in the expansion of $\mathbf{v}_h$ (to be used in (3f)) has $6(N - N_D)$ DoF's. The same applies for approximations within the space

Table 3
Relative errors for the $\mathbf{OFE}_1/\mathrm{OFE}_0$ pair.

$\Delta = 0$	$\Delta = 0.5$	$\Delta = 0.7$
$\varepsilon_{\mathbf{u}}(h) \simeq D_1 h^{1.8880}$	$\varepsilon_{\mathbf{u}}(h) \simeq D_2 h^{1.0257}$	$\varepsilon_{\mathbf{u}}(h) \simeq D_3 h^{1.4442}$
$\varepsilon_p(h) \simeq D_4 h^{1.0187}$	$\varepsilon_p(h) \simeq D_5 h^{0.8126}$	$\varepsilon_p(h) \simeq D_6 h^{1.1286}$

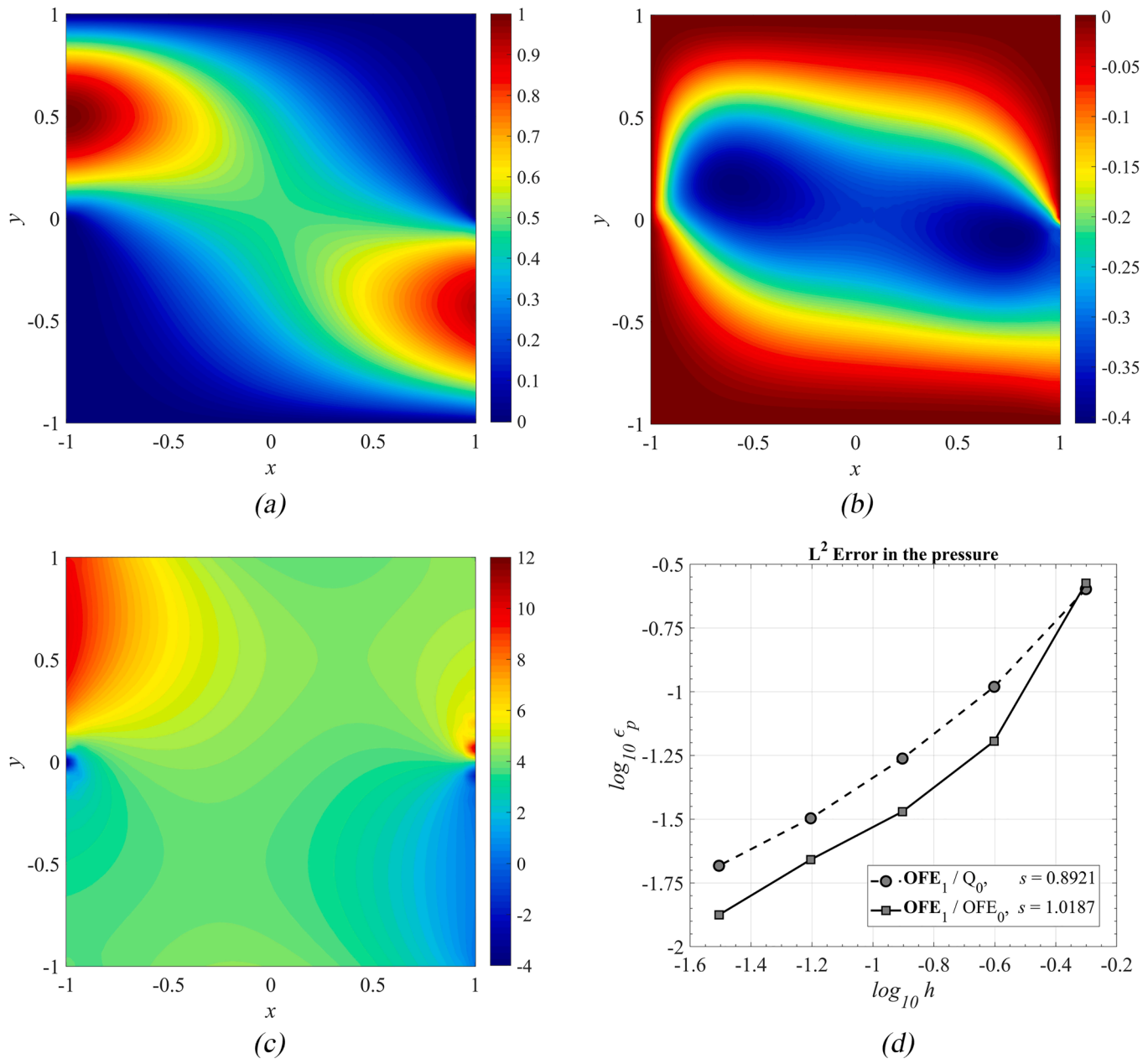

Fig. 11. Finite element solution, calculated using the $\mathbf{OFE}_1/\mathrm{OFE}_0$ pair, using a uniform mesh formed by 32×32 square elements. *(a)* Horizontal component of the velocity field. *(b)* Vertical component of the velocity field. *(c)* The pressure field. *(d)* Error in the pressure for a sequence of uniform meshes ($\Delta = 0$), using the $\mathbf{OFE}_1/Q_0$ pair (black curve in Fig. 8b, shown as a dashed curve here), and using the $\mathbf{OFE}_1/\mathrm{OFE}_0$ pair (black curve in Fig. 10c). The slopes s are taken from Tables 2 and 3.

$\mathbf{OFE}_2$. Substituting the expressions from (3f), the inf-sup condition (2e) becomes:

There is some constant $\beta_h > 0$ such that

$$\inf_{\widetilde{\mathbf{Q}}\in\mathbb{R}^M\setminus\{0\}} \sup_{\widetilde{\mathbf{V}}\in\mathbb{R}^K\setminus\{0\}} \frac{\widetilde{\mathbf{Q}}^T\ \bar{\mathbb{B}}\ \widetilde{\mathbf{V}}}{\sqrt{\widetilde{\mathbf{Q}}^T\ \bar{\mathbb{Y}}\ \widetilde{\mathbf{Q}}}\sqrt{\widetilde{\mathbf{V}}^T\ \bar{\mathbb{K}}\ \widetilde{\mathbf{V}}}} \geq \beta_h, \tag{3g}$$

where K and M denote the dimensions of vectors $\widetilde{\mathbf{V}}$ (after treating the zero DoF's, as described above) and $\widetilde{\mathbf{Q}}$, respectively. We assume that $\ker\ \bar{\mathbb{B}}^T = \{\mathbf{0}\}$, since if $\ker\ \bar{\mathbb{B}}^T \neq \{\mathbf{0}\}$ we see that (3g) cannot be satisfied. Then we consider

$$\inf_{\widetilde{\mathbf{Q}}\in\mathbb{R}^M\setminus\{0\}} \sup_{\widetilde{\mathbf{V}}\in\mathbb{R}^K\setminus\{0\}} \frac{\widetilde{\mathbf{Q}}^T\ \bar{\mathbb{B}}\ \widetilde{\mathbf{V}}}{\sqrt{\widetilde{\mathbf{Q}}^T\ \bar{\mathbb{Y}}\ \widetilde{\mathbf{Q}}}\sqrt{\widetilde{\mathbf{V}}^T\ \bar{\mathbb{K}}\ \widetilde{\mathbf{V}}}} = \sqrt{\mu_{\min}(h)},$$

where $\mu_{\min}(h)$ is the smallest eigenvalue in the problem:

$$\bar{\mathbb{B}}\ \bar{\mathbb{K}}^{-1}\ \bar{\mathbb{B}}^T\ \widetilde{\mathbf{Q}} = \mu\ \bar{\mathbb{Y}}\ \widetilde{\mathbf{Q}}, \tag{3h}$$

see [3,14]. If $\mu_{\min}(h)$ is positive, we can choose the constant β_h in (3g) as $\beta_h = \sqrt{\mu_{\min}(h)}$. In this way, (3g) and ultimately (2e) are satisfied. For a given partition $\mathscr{C}_h$ (characterized by a discretization length h), the eigenproblem (3h) tells if the discrete Navier-Stokes problem is free of spurious pressure solutions, i.e., if the pressure field is unique. The idea behind the Chapelle-Bathe inf-sup testing is:

1. Consider a sequence of partitions $\mathscr{C}_h$ for decreasing values of h (i.e., the meshes are getting finer and finer);
2. For each partition $\mathscr{C}_h$, compute the value of $\beta_h = \sqrt{\mu_{\min}(h)}$ in (3h);
3. Plot the sequence of values β_h in a graph as h decreases. If the curve reaches a 'plateau' (i.e., the values of β_h are 'locked' above a certain

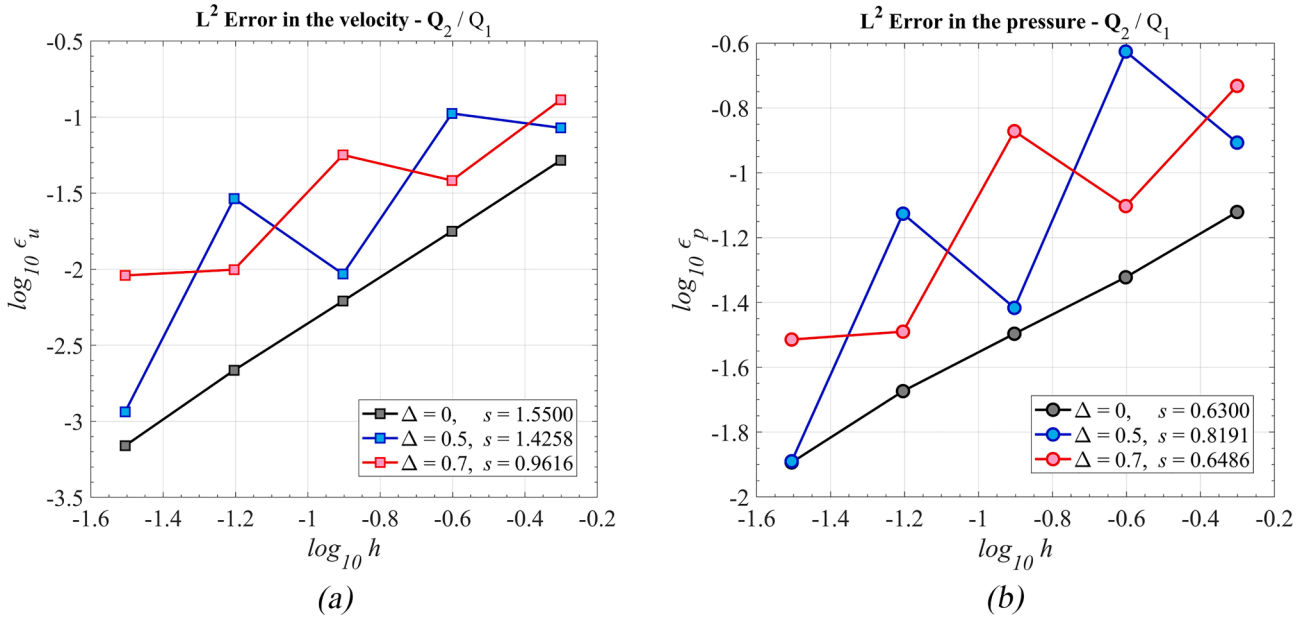

Fig. 12. Convergence curves for the Q_2/Q_1 pair. The errors are calculated with respect to the reference solution from Fig. 4 (which uses a more refined mesh), using (4c). *(a)* Error in the velocity. *(b)* Error in the pressure. The slopes s are taken from Table 4, and Δ is the mesh distortion parameter.

positive value), we conclude that β_h will be positive for all decreasing h.

Of course, if the curve in Step 3 exhibits the 'plateau' profile – that is, the inf-sup test is passed – we can only conclude that we are able to find an inf-sup constant β that is independent of h for the specific sequence of meshes used. For this reason, we conservatively repeat the test using also other sequences of meshes, like distorted meshes, and then if the test is passed for a sufficient number of discretizations, it is our experience that the element used is stable, and hence the solutions will not provide spurious pressures.

Table 4
Relative errors for the Q_2/Q_1 pair.

$\Delta = 0$	$\Delta = 0.5$	$\Delta = 0.7$
$\varepsilon_{\mathbf{u}}(h) \simeq E_1 h^{1.5500}$	$\varepsilon_{\mathbf{u}}(h) \simeq E_2 h^{1.4258}$	$\varepsilon_{\mathbf{u}}(h) \simeq E_3 h^{0.9616}$
$\varepsilon_p(h) \simeq E_4 h^{0.6300}$	$\varepsilon_p(h) \simeq E_5 h^{0.8191}$	$\varepsilon_p(h) \simeq E_6 h^{0.6486}$

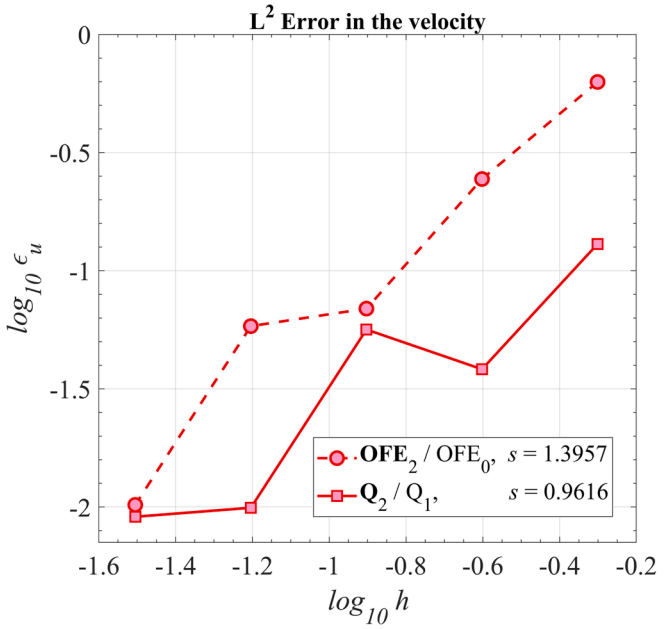

Fig. 13. Convergence curves for the $\mathbf{OFE}_2/\mathrm{OFE}_0$ and Q_2/Q_1 pairs, when the mesh distortion parameter is given by $\Delta = 0.7$. The errors in the velocity are calculated with respect to the reference solution from Fig. 4, using (4c).

4. Numerical solutions on convergence and inf-sup stability

This section presents a study of the convergence and inf-sup stability of the finite element spaces under consideration. We are interested in solving the homogeneous Stokes system, posed in the square domain $\Omega = (-1,1)\times(-1,1)$:

Find $(\mathbf{u},p)$ such that

$$\begin{aligned} -\nabla^2\mathbf{u} + \nabla p &= \mathbf{0}, \quad \text{in } \Omega, \\ \nabla\cdot\mathbf{u} &= 0, \quad \text{in } \Omega, \\ \mathbf{u} &= \mathbf{g}_D, \quad \text{on } \Gamma_D, \\ \hat{\mathbf{n}}\cdot\bar{\bar{\boldsymbol{\sigma}}} &= \mathbf{0}, \quad \text{on } \Gamma_N. \end{aligned} \tag{4a}$$

The Dirichlet boundary Γ_D corresponds to the top, bottom, and left walls, in addition to the upper half of the right wall, see Fig. 3. The Neumann boundary Γ_N corresponds to the lower half of the right wall. The essential boundary conditions are given by the 'no-slip' condition $\mathbf{g}_D = [0,0]^T$ along the top and bottom walls; along the left wall ($x = -1$) they are given by:

$$\mathbf{g}_D = \begin{cases} [0,0]^T, & \text{if } -1 \le y < 0, \\ [4y(1-y),0]^T, & \text{if } 0 \le y \le 1, \end{cases} \tag{4b}$$

and along the upper half of the right wall ($x = 1$), they are also given by $\mathbf{g}_D = [0,0]^T$, if $0 \le y \le 1$. This problem describes, in a very simplified manner, the flow of a viscous fluid that enters the domain Ω through the upper half of the left wall (the 'inlet'), and leaves the domain through the lower half of the right wall (the 'outlet'), see Fig. 4d. The weak form of (4a) can be obtained from the formulation for the complete Navier-Stokes problem (discussed in Sections 2.2 and 2.3) by omitting the nonlinear terms. The problem (4a)-(4b) does not admit analytical solution, and so the results calculated in the next sections will be compared

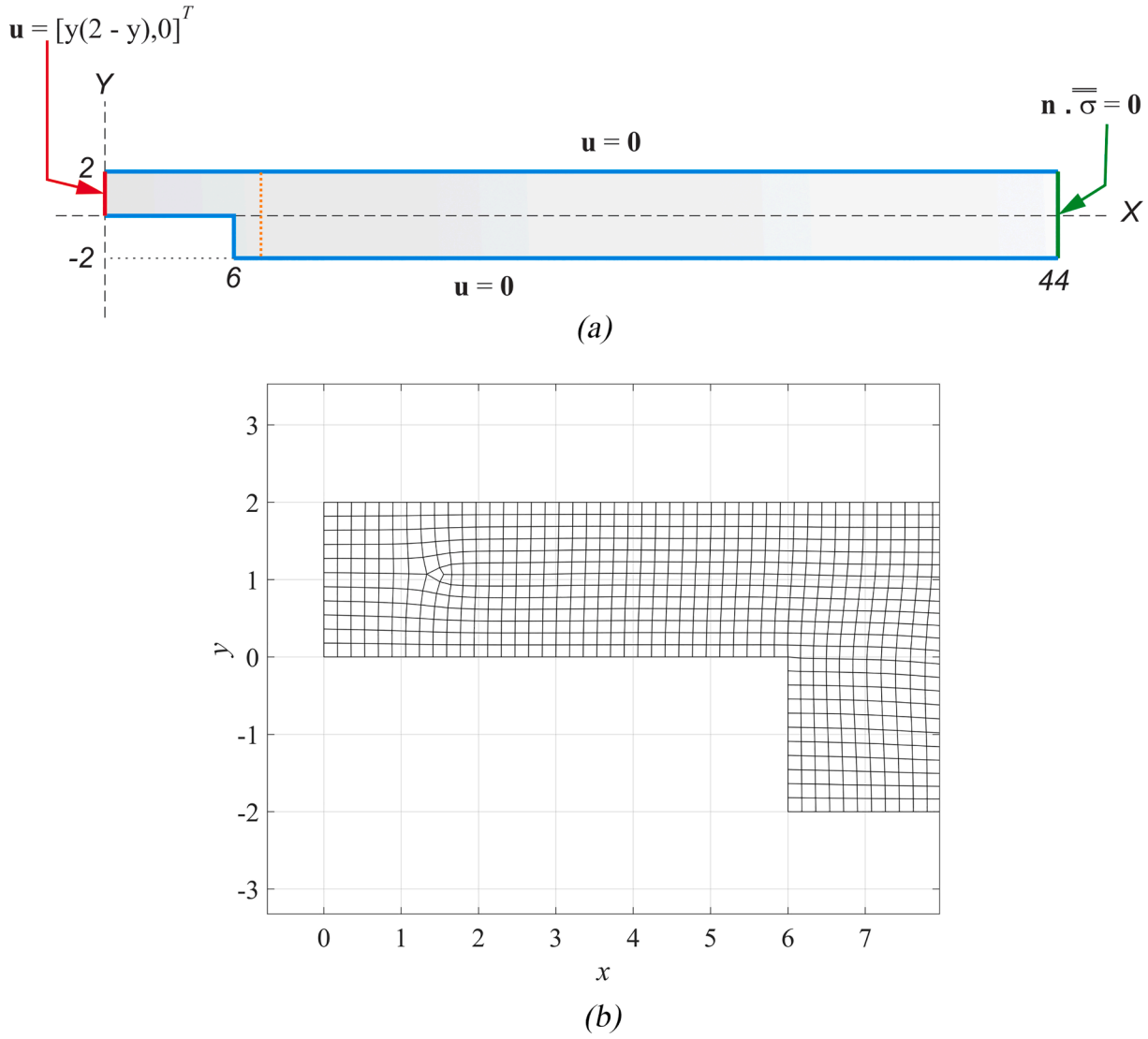

Fig. 14. *(a)* Geometry (dimensionless units) and boundary conditions relative to the problem from Section 4.4. Inlet and outlet shown in red and green, respectively; no-slip walls shown in blue. *(b)* Portion of the mesh with 5,579 cells used for the different types of finite elements. (For interpretation of the references to colour in this figure legend, the reader is referred to the web version of this article.)

with a finite element reference solution $(\mathbf{u}_{Ref}, p_{Ref})$. This solution is obtained by solving problem (4a)-(4b) in a very fine uniform mesh of 128×128 elements (length and height of Ω subdivided equally). The components of the velocity are approximated by biquadratic basis functions (traditional 9-node elements), whereas the pressure is approximated by bilinear basis functions (traditional 4-node elements). This pair is sometimes referred to in the literature as the $\boldsymbol{Q}_2/Q_1$ element, and it passes the inf-sup condition and test [3,20]. The reference solution is illustrated in Fig. 4.

4.1. Discontinuous pressure approximations

In this subsection we first solve problem (4a)-(4b) using bilinear basis functions (traditional 4-node elements) for the velocity, and constant basis functions for the pressure (which leads to a piecewise constant, and hence discontinuous approximation). This pair is sometimes referred to in the literature as the $\boldsymbol{Q}_1/Q_0$ element [20]. We again use uniform meshes, i.e., the square domain Ω is uniformly divided into $N \times N$ elements (i.e., little squares), where $N \in \{4, 8, 16, 32, 64\}$. The discretization length h is defined as the side of Ω divided by N, i.e., $h = 2/N$. This pair is easy to code, and for a given fixed mesh (characterized by a fixed h), reasonable solutions for the velocity field $\mathbf{u}_h$ can be obtained (see Fig. 5), although the pressure p_h may become contaminated by the checkerboard pattern [3,20], see Fig. 5c. Moreover, for each fixed mesh we can find a positive constant β_h that satisfies the inf-sup condition stated in Section 3.4. However, as the meshes become more refined (i.e., as h decreases), these constants β_h become progressively smaller, as attested by Fig. 5d. So the pair $\boldsymbol{Q}_1/Q_0$ does not pass the inf-sup test.

We propose a modification: Instead of using bilinear basis functions (traditional 4-node elements) for approximating the velocity, we use the OFE scheme with monomials of degree 1 in the local bases, i.e., the space $\mathbf{OFE}_1$ (Section 3.2). The pressure is still approximated by piecewise constant functions. The resulting pair is denoted $\mathbf{OFE}_1/Q_0$. In what regards the Dirichlet conditions, they are imposed directly in the OFE.

Since a node I located at $\mathbf{x}_I \in \Gamma_D$ carries 3 DoF's per velocity component, we make the first DoF (associated with the constant term in the local basis) equal to the prescribed value of the field at the location $\mathbf{x}_I$. The other DoF's are taken to be zero, see Section 3.1. We now solve problem (4a)-(4b) and perform the inf-sup test using this element. We again obtain a good solution for the velocity $\mathbf{u}_h$, but this time the pressure p_h is not contaminated by the checkerboard pattern, despite the fact

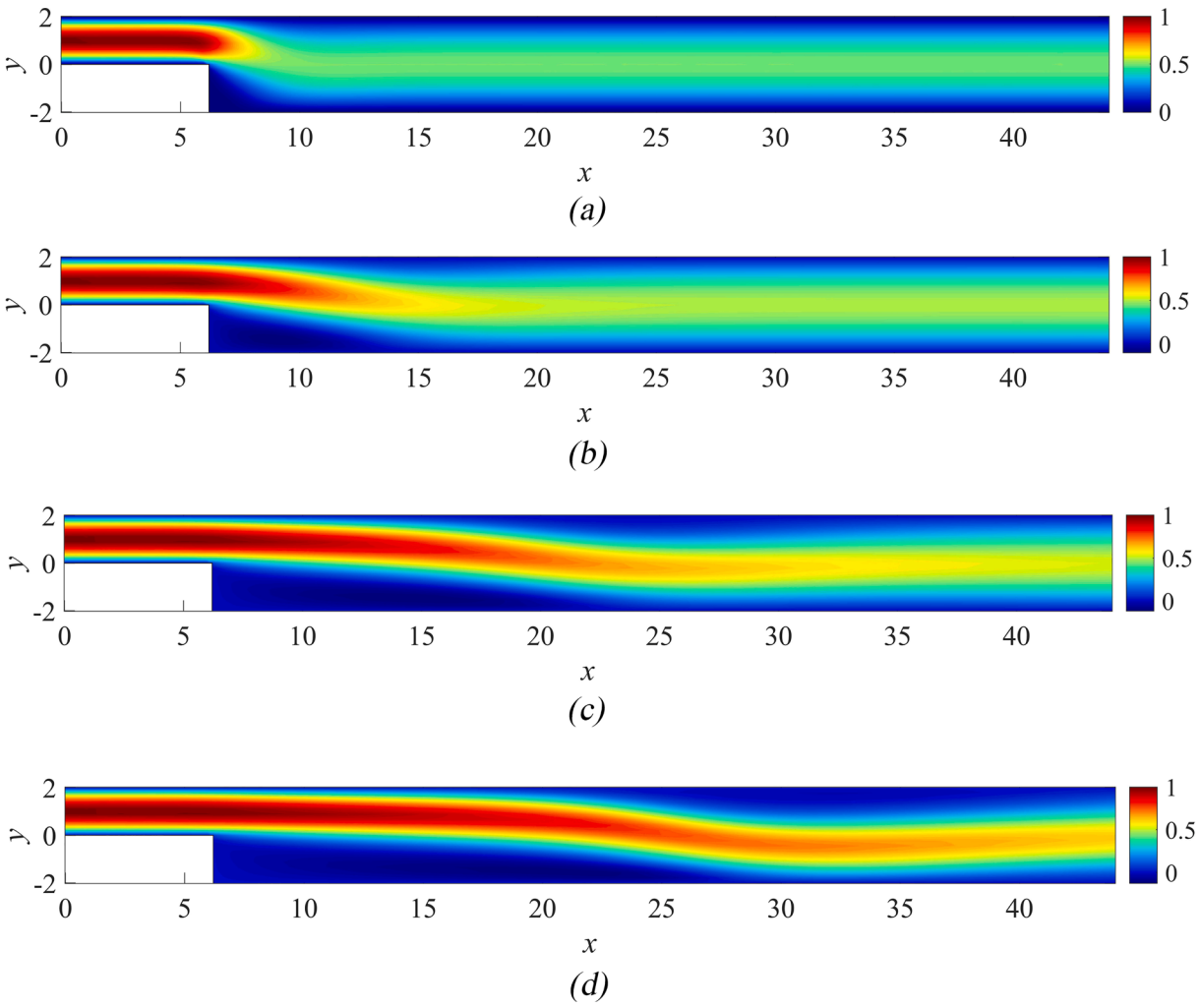

Fig. 15. The horizontal component $u_{h,1}$ provided by the $\mathbf{OFE}_1/\mathrm{OFE}_0$ pair. *(a)* Solution at $Re = 5$. *(b)* Solution at $Re = 50$. *(c)* Solution at $Re = 150$. *(d)* Solution at $Re = 250$.

we are still using a discontinuous pressure approximation, see Fig. 6. Moreover, it can be seen that the $\mathbf{OFE}_1/Q_0$ pair passes the inf-sup test, since the constants β_h attain a plateau, and do not decrease towards zero (see Fig. 5d).

Please notice that in the integration of the weak forms discretized with the $\boldsymbol{Q}_1/Q_0$ and $\mathbf{OFE}_1/Q_0$ pairs, we use the same rule in both cases (Gaussian quadrature, 3 x 3 points per element, see Section 3.3), so that the effort in the evaluation of the matrices is the same. The only difference is that, in the OFE scheme, we need to calculate the maximum distance r_I at each node (see (3a)). This is a strong argument in favor of our OFE basis functions.

In order to verify the behavior of the $\mathbf{OFE}_1/Q_0$ pair on distorted meshes, we begin by constructing these meshes. First, we consider the square domain $\bar{\Omega} = [-1,1] \times [-1,1]$, and subdivide each side into $N = 2$ equal segments, thus resulting in 2×2 smaller squares, see Fig. 7a. Second, the middle horizontal segment is tilted upwards, so that the point $(1,0)$ is moved to the point $(1,\Delta)$. And lastly, the middle vertical segment is tilted to the right, so that the point $(0,1)$ is moved to the point $(\Delta,1)$, see Fig. 7b. The parameter Δ controls the distortion of the mesh; the greater the value of Δ, the more distorted the mesh becomes. Of course, when $\Delta = 0$, the mesh has no distortion. We now subdivide each one of the four cells into four other cells, by uniting the midpoints of their sides that lie opposite to each other. It can be verified that each side of the original square Ω has been divided into $N = 4$ segments. This results in a new mesh with 4×4 new cells, see Fig. 7c. The process continues, as the cells are further subdivided. For each N, we again define the discretization length as $h = 2/N$, and calculate the discrete solution $(\mathbf{u}_h, p_h)$ using the $\mathbf{OFE}_1/Q_0$ pair. The relative errors in the $\mathbf{L}^2$ norm (for the velocity field) and in the L^2 norm (for the pressure) are calculated as

$$\varepsilon_{\mathbf{u}}(h) = \frac{\|\mathbf{u}_h - \mathbf{u}_{Ref}\|_{\mathbf{L}^2(\Omega)}}{\|\mathbf{u}_{Ref}\|_{\mathbf{L}^2(\Omega)}}, \quad \text{and} \quad \varepsilon_p(h) = \frac{\|p_h - p_{Ref}\|_{L^2(\Omega)}}{\|p_{Ref}\|_{L^2(\Omega)}}. \tag{4c}$$

The results are displayed in Fig. 8. We first obtain a sequence of undistorted meshes ($\Delta = 0$), for $N \in \{4, 8, 16, 32, 64\}$, and calculate (4c) for each h. Then we repeat the process for a sequence of distorted meshes ($\Delta = 0.5$), and again for a sequence of very distorted meshes ($\Delta = 0.7$), see Fig. 9. We observe that the errors $\varepsilon_{\mathbf{u}}$ and ε_p converge 'smoothly' for the sequence of undistorted meshes. For the sequences of distorted meshes, despite the erratic behavior, there is still convergence. A linear regression applied to the graphs from Fig. 8 allows us to deduce the approximate behavior of the errors in (4c), see Table 2. Of course, $C_1, \cdots, C_6$ are positive constants. This table reveals that, even for very distorted meshes, reasonable convergence rates can be obtained.

4.2. Continuous pressure approximations

In this section we shall examine a new pair: The components of the velocity field $\mathbf{u}_h$ are still approximated using the OFE scheme with monomials of degree 1 in the local bases (i.e., $\mathbf{u}_h$ is calculated within the space $\mathbf{OFE}_1$, as in Section 4.1), whereas the pressure p_h will be

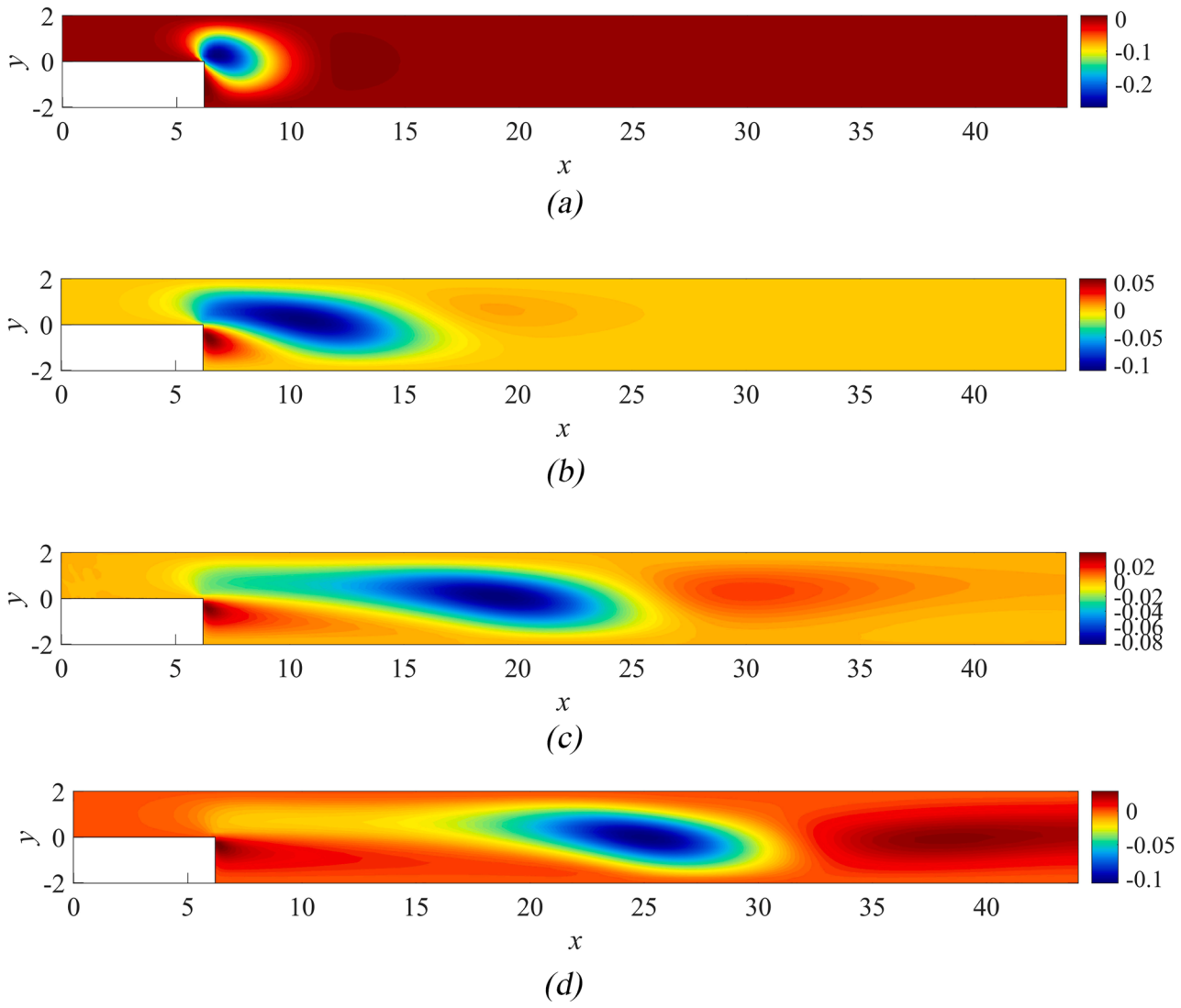

Fig. 16. The vertical component $u_{h,2}$ provided by the $\mathbf{OFE}_1/\mathrm{OFE}_0$ pair. *(a)* Solution at $Re = 5$. *(b)* Solution at $Re = 50$. *(c)* Solution at $Re = 150$. *(d)* Solution at $Re = 250$.

approximated using the OFE scheme with monomials of degree 0 in the local bases (i.e., p_h will be calculated within the space OFE_0, see Section 3.2). The resulting pair is denoted $\mathbf{OFE}_1/\mathrm{OFE}_0$. The first step is to examine the inf-sup stability of this pair. We set up a sequence of uniform meshes by subdividing the domain Ω into $N \times N$ squares, for $N \in \{4, 8, 16, 32, 64\}$. The discretization length h is defined as in Section 4.1. The result is displayed in Fig. 10a, which shows that the pair $\mathbf{OFE}_1/\mathrm{OFE}_0$ clearly passed the inf-sup test, since the constants β_h again stabilize at a positive value away from zero. The results for the convergence analysis are shown in Fig. 10b and in Fig. 10c. We obtained a similar behavior as that from the previous section, i.e., the errors (4c) converge 'smoothly' for the sequence of undistorted meshes, and converge 'erratically' for the sequences of distorted meshes. The approximate convergence rates of the errors are shown in Table 3 ($D_1, \cdots, D_6$ are positive constants).

If we compare the results in Table 2 and in Table 3, we see that the convergence rates for the error in the velocity $\varepsilon_{\mathbf{u}}$ and in the pressure ε_p are almost equal. This is reasonable, since the velocity field is approximated in the same way in both cases, whereas the pressure is approximated by zero-order basis functions from traditional FEM (which happen to be discontinuous) in the first case, and by zero-order basis functions from the OFE (which happen to be continuous) in the second case. When precision is not required for the pressure solution, the $\mathbf{OFE}_1/Q_0$ pair becomes an attractive choice, since it is easier to implement than the $\mathbf{OFE}_1/\mathrm{OFE}_0$ pair. Both pairs pass the inf-sup test, and present a similar cost (the first uses 1 DoF per element for approximating the pressure, whereas the second uses 1 DoF per node).

According to Figs. 11a and 11b, the velocity solutions for the $\mathbf{OFE}_1/\mathrm{OFE}_0$ pair are similar to those for the $\mathbf{OFE}_1/Q_0$ pair (see Figs. 6a and 6b). However, a comparison between Fig. 11c and Fig. 6c shows that the approximation for the pressure is better when the $\mathbf{OFE}_1/\mathrm{OFE}_0$ pair is used. This is expected, as it uses a continuous approximation for the pressure. We point out that, despite presenting a similar rate of convergence, the error in the pressure ε_p for the $\mathbf{OFE}_1/\mathrm{OFE}_0$ pair is smaller than that for the $\mathbf{OFE}_1/Q_0$ pair, as it should. This can be verified when we plot the error ε_p for both cases and for a sequence of undistorted meshes ($\Delta = 0$), see Fig. 11d (in other words, the constants C_4 in Table 2 and D_4 in Table 3 are different).

We also performed a convergence analysis for the traditional $\boldsymbol{Q}_2/Q_1$ pair, in order to see how it behaves in distorted meshes, see Fig. 12. We did as in the previous two cases, i.e., we considered a sequence of meshes with $N \times N$ subdivisions, where $N \in \{4, 8, 16, 32, 64\}$. It can be observed that the errors (4c) once more converge 'smoothly' for the sequence of undistorted meshes, and converge 'erratically' for the sequences of distorted meshes. Table 4 shows the approximate behavior of the errors for this element ($E_1, \cdots, E_6$ are positive constants).

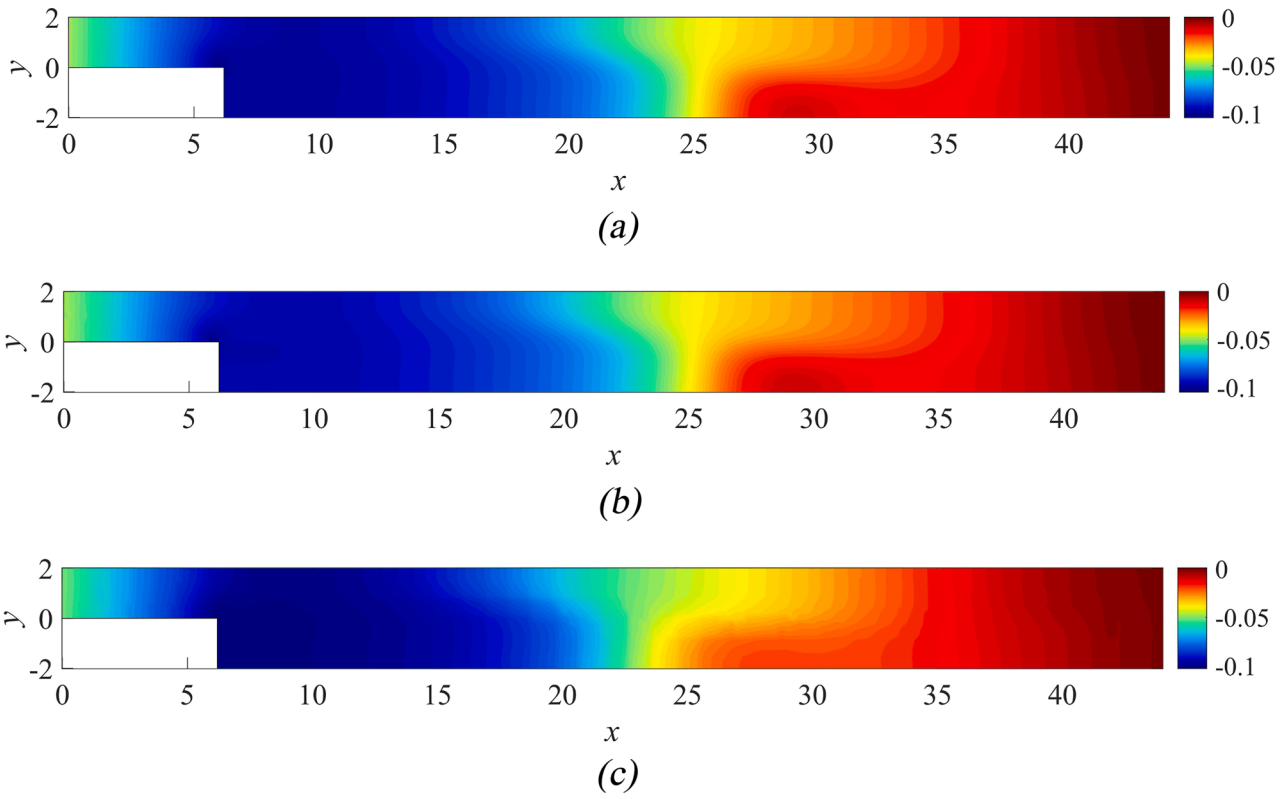

Fig. 17. The pressure field p_h at $Re = 250$. *(a)* Reference solution provided by the $\boldsymbol{Q}_2/Q_1$ pair. *(b)* Solution provided by the $\mathbf{OFE}_1/\mathrm{OFE}_0$ pair (continuous approximation). *(c)* Solution provided by the $\mathbf{OFE}_1/Q_0$ pair (discontinuous approximation).

A comparison of Table 4 with Tables 2 and 3 reveals two characteristics. First, when uniform meshes ($\Delta = 0$) are employed, the convergence rates for the $\boldsymbol{Q}_2/Q_1$ pair are smaller than those for the $\mathbf{OFE}_1/Q_0$ and $\mathbf{OFE}_1/\mathrm{OFE}_0$ pairs. This is remarkable, since in the $\boldsymbol{Q}_2/Q_1$ scheme the velocity field is approximated by second-order (biquadratic) basis functions from traditional FEM, whereas in the $\mathbf{OFE}_1/Q_0$ and $\mathbf{OFE}_1/\mathrm{OFE}_0$ schemes the velocity field is approximated by first-order (linear) local basis functions. And second, the degradation in the convergence rate for $\varepsilon_{\mathbf{u}}$ when very distorted meshes are used ($\Delta = 0.7$) is slightly larger for the traditional biquadratic 9-node element ($\boldsymbol{Q}_2$) than for the linear OFE element ($\mathbf{OFE}_1$).

We conclude this section by observing that the pairs we have found (namely, the $\mathbf{OFE}_1/Q_0$ and the $\mathbf{OFE}_1/\mathrm{OFE}_0$):

- are low-order (zero and first-order basis functions, at most, which lead to a low number of DoF's);
- are stable (i.e., they pass the inf-sup test);
- are less sensitive to mesh distortions than the traditional $\boldsymbol{Q}_2/Q_1$ pair (to obtain less distortion sensitivity for the OFE, the nodal basis functions need to be increased as shown in the paper);
- do not resort to artifices like 'bubble functions' or 'macroelements' (in which the pressure is approximated by a given mesh and the velocity is approximated by a more refined mesh, see [3,20]).

4.3. Higher-order velocity approximations and the AMORE paradigm

The first-order approximations based on the $\mathbf{OFE}_1/Q_0$ and $\mathbf{OFE}_1/\mathrm{OFE}_0$ pairs lead to a reasonably low number of DoF's (as described above), and require few integration points (3 x 3 points per element). These features allow them to be used efficiently in the whole computational domain Ω, i.e., in all elements of the partition $\mathscr{C}_h$, as we do in this paper.

In second-order approximations, the components $u_{h,1}$ and $u_{h,2}$ of the velocity field are calculated within the space OFE_2 (which uses quadratic terms in the local bases, see Section 3.2). When the pressure p_h is calculated within the space OFE_0 (which uses a constant term in the local bases), the resulting pair is denoted $\mathbf{OFE}_2/\mathrm{OFE}_0$. Fig. 10a shows that this pair passes the inf-sup test, since the constants β_h do not decay towards zero.

The $\mathbf{OFE}_2/\mathrm{OFE}_0$ pair can in principle also be used in the whole computational domain, if coarser meshes are used (because this pair requires 6 DoF's per node for each component in the approximation of the velocity), see Section 4.5 below. However, the primary purpose of these elements is to be used within the AMORE paradigm (Automatic Meshing with Overlapping and Regular Elements) [6,27,28]. The idea is to produce a partition $\mathscr{C}_h$ in such a way that the cells in the central portions of the domain Ω are uniformly distributed, i.e., in two-dimensional analyses these interior cells are all square as seen in an undistorted finite-difference grid. The remaining parts of Ω closer to boundaries, interfaces and holes are then meshed with not-so-regular, possibly very distorted cells. In the discretization, traditional low-order finite element spaces are used in the regular undistorted elements (in the bulk of the domain), whereas the OFE spaces are used in the distorted elements (close to boundaries). A special procedure of coupling elements is devised to couple the approximations within those square regular elements with the OFE elements [6].

The AMORE paradigm has been successfully employed in the solution of problems of linear elastic solid mechanics [36]. Since the basic premise of the paradigm is to use traditional low-order elements in the uniform mesh set up in the bulk of the domain, in two-dimensional analyses, traditional 4-node elements, frequently with incompatible modes, are chosen [36]. Of course, for problems in solid and fluid mechanics of incompressible media, the traditional low-order $\boldsymbol{Q}_1/Q_0$ pair cannot be used since it does not pass the inf-sup test and yields pressure solutions contaminated by the checkerboard pattern (see Section 4.1). The $\mathbf{OFE}_1/Q_0$ and $\mathbf{OFE}_1/\mathrm{OFE}_0$ pairs, in solid mechanics possibly with incompatible modes, may be a good choice. In fluid mechanics control volume elements may be preferred for the interior domain. But

regardless of which elements are used in the uniform mesh, our second-order $\mathbf{OFE}_2/\mathrm{OFE}_0$ pair can be used in the remaining distorted elements close to the boundaries.

Since the $\mathbf{OFE}_2/\mathrm{OFE}_0$ pair will be used primarily in distorted elements, we solved problem (4a)-(4b), again considering a sequence of very distorted meshes ($\Delta = 0.7$) with $N \times N$ subdivisions each, where $N \in \{4, 8, 16, 32, 64\}$. In Fig. 13 we compare the errors (4c) provided by the $\mathbf{OFE}_2/\mathrm{OFE}_0$ pair with those provided by the $\boldsymbol{Q}_2/Q_1$ pair (red curve in Fig.12a). We see that these errors are similar for a sufficiently small h. However, the convergence of the error in the $\mathbf{OFE}_2/\mathrm{OFE}_0$ pair is less erratic than the convergence of the error in the $\boldsymbol{Q}_2/Q_1$ pair. Indeed, a linear regression reveals that the error provided by the $\mathbf{OFE}_2/\mathrm{OFE}_0$ pair behaves as $\varepsilon_{\mathbf{u}}(h) \simeq Ch^{1.3957}$, whereas the error provided by the $\boldsymbol{Q}_2/Q_1$ pair behaves as $\varepsilon_{\mathbf{u}}(h) \simeq Dh^{0.9616}$, where C and D are positive constants (see the first row in Table 4).

4.4. Navier-Stokes flow over a step

This benchmark problem describes the flow of a viscous fluid over a backward facing step, see Fig. 14a. The fluid enters the domain through the leftmost wall (line segment $x = 0$ and $0 \leq y \leq 2$). Along this line segment, the prescribed inflow velocity is given by $\mathbf{g}_D = [y(2-y), 0]^T$. On the rightmost wall (line segment $x = 44$ and $-2 < y < 2$), we impose the homogeneous Neumann condition ($\hat{\mathbf{n}} \cdot \bar{\bar{\boldsymbol{\sigma}}} = 0$). Finally, the no-slip condition $\mathbf{g}_D = [0, 0]^T$ is prescribed along the other walls.

The goal of this Section is to solve the Navier-Stokes problem (2a), characterized by Reynolds numbers between $Re = 5$ and $Re = 250$. The body force is assumed to be zero, i.e., $\mathbf{f} = 0$. The mesh is formed by

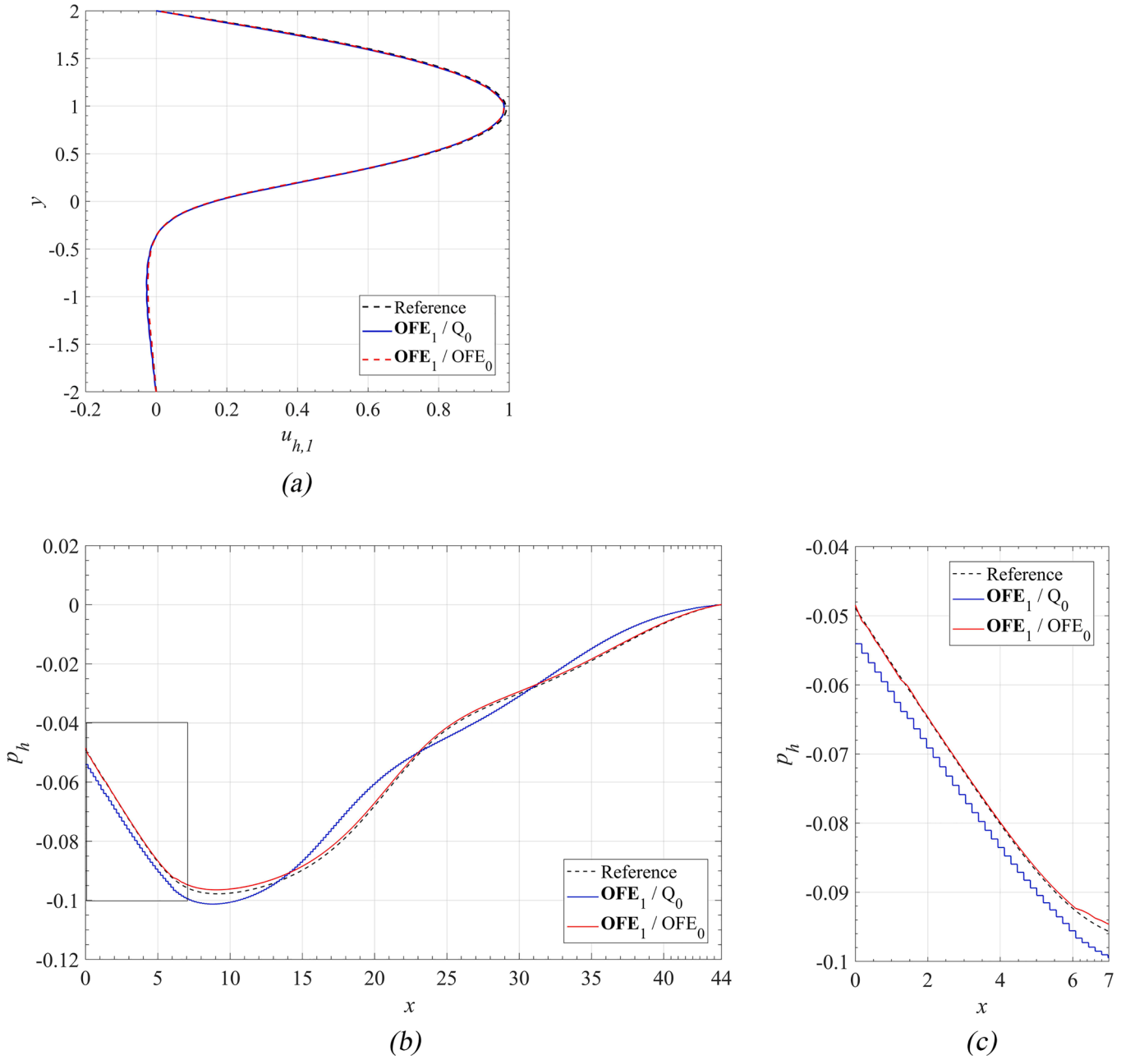

Fig. 18. Field profiles at $Re = 250$, provided by the $\mathbf{OFE}_1/Q_0$ and $\mathbf{OFE}_1/\mathrm{OFE}_0$ pairs. *(a)* Horizontal component of the velocity field $u_{h,1}$ calculated along the vertical line segment $x = 7$ and $-2 \leq y \leq 2$ (dotted orange line in Fig. 14a). *(b)* Pressure field p_h along the top wall (horizontal line segment $0 \leq x \leq 44$ and $y = 2$). *(c)* Zooming in on the region marked with a rectangle in Fig. 18b. Reference solution given by the $\boldsymbol{Q}_2/Q_1$ pair, using the mesh of cells in Fig. 14b. (For interpretation of the references to colour in this figure legend, the reader is referred to the web version of this article.)

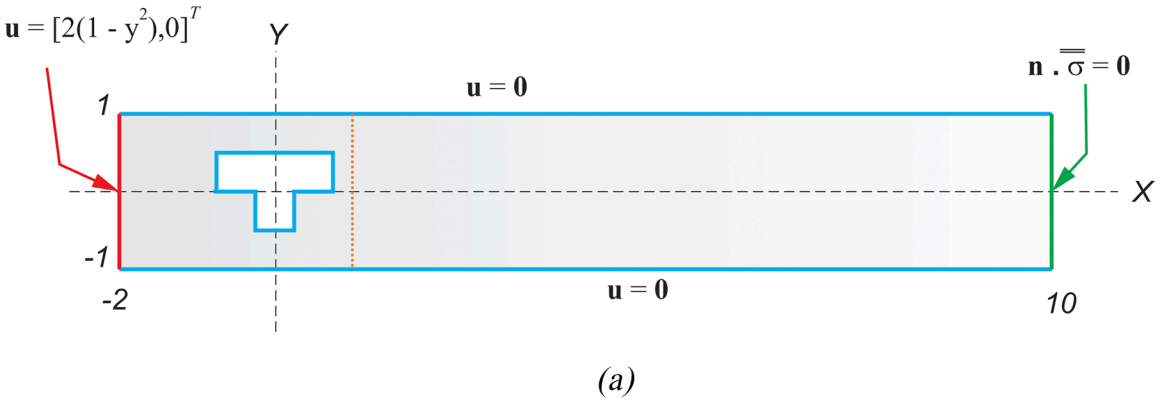

(a)

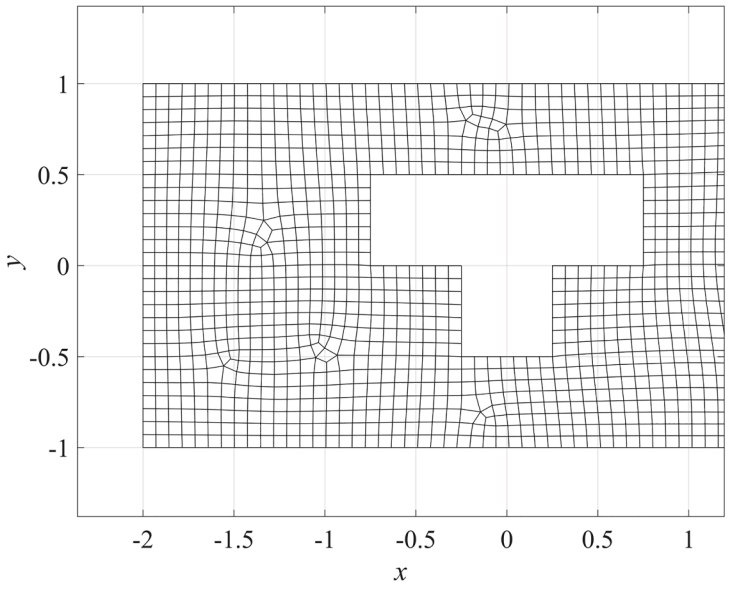

(b)

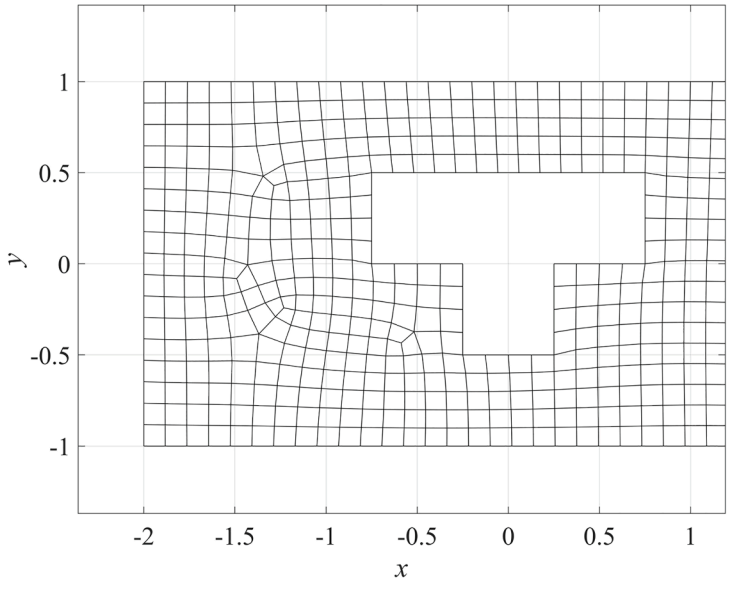

(c)

Fig. 19. *(a)* Geometry (dimensionless units) and boundary conditions relative to the problem from Section 4.5. Inlet and outlet shown in red and green, respectively; no-slip walls shown in blue. *(b)* Portion of the mesh with 4,767 cells used for the different types of finite elements. *(c)* Portion of a coarser mesh, with 1,781 cells. (For interpretation of the references to colour in this figure legend, the reader is referred to the web version of this article.)

5,579 cells, a portion of which is illustrated in Fig. 14b. The discretized components $u_{h,1}$ and $u_{h,2}$ provided by the $\mathbf{OFE}_1/\mathrm{OFE}_0$ pair are plotted in Figs. 15 and 16, respectively. Figures 17b and 17c illustrate the pressure field p_h provided by the $\mathbf{OFE}_1/\mathrm{OFE}_0$ pair (continuous pressure) and by the $\mathbf{OFE}_1/Q_0$ pair (discontinuous pressure), respectively, for $Re = 250$. We note an almost perfect agreement between the reference $\boldsymbol{Q}_2/Q_1$ and $\mathbf{OFE}_1/\mathrm{OFE}_0$ pressure solutions (Figs. 17a and 17b, respectively).

We see that the velocity solutions calculated using the $\mathbf{OFE}_1/\mathrm{OFE}_0$ and the $\mathbf{OFE}_1/Q_0$ pairs look similar to each other (see Fig. 18a, which shows the component $u_{h,1}$ along the vertical segment $x = 7$ and $-2 \leq y \leq 2$). However, when we examine the pressure profile along the top wall (horizontal line segment $0 \leq x \leq 44$ and $y = 2$) in Figs. 18b and 18c, the 'staircase' appearance of the solution provided by the $\mathbf{OFE}_1/Q_0$ pair becomes evident. This is expected, since this pair employs constant basis functions, leading to a piecewise constant (discontinuous) approximation. The pressure solution provided by the $\mathbf{OFE}_1/\mathrm{OFE}_0$ pair agrees well with the reference solution, and in a sense, the solution provided by the $\mathbf{OFE}_1/Q_0$ pair also does, despite the 'staircase' appearance.

4.5. Navier-Stokes flow around a T-shaped object

In this section we examine the flow along a channel in which a T-shaped object has been embedded, see Fig. 19a. The prescribed inflow velocity along the inlet (line segment $x = -2$ and $-1 \leq y \leq 1$) is $\mathbf{g}_D = [2(1+y)(1-y), 0]^T$. On the rightmost wall (line segment $x = 10$ and $-1 < y < 1$), we impose the homogeneous Neumann condition ($\hat{\mathbf{n}} \cdot \bar{\bar{\boldsymbol{\sigma}}} = 0$). Finally, the no-slip condition $\mathbf{g}_D = [0, 0]^T$ is prescribed along the other walls, in addition to the contour of the object. We solve the Navier-Stokes problem (2a), characterized by a Reynolds number equal to $Re = 50$. The body force is again assumed to be zero, i.e., $\mathbf{f} = 0$. Two different solution schemes are used:

Linear approximation ($\mathbf{OFE}_1/\mathrm{OFE}_0$ pair): Mesh containing 4,767 cells, leading to 34,979 DoF's;

Quadratic approximation ($\mathbf{OFE}_2/\mathrm{OFE}_0$ pair): Mesh containing 1,781 cells, leading to 24,947 DoF's.

The velocity and pressure fields corresponding to the $\mathbf{OFE}_1/\mathrm{OFE}_0$ pair are shown in Fig. 20. The fields corresponding to the $\mathbf{OFE}_2/\mathrm{OFE}_0$ pair (not shown) are very similar. Please note that the quadratic approximation uses a much coarser mesh (Fig. 19c), having approximately one third of the number of cells in the mesh used for the linear approximation (Fig. 19b). Moreover, the quadratic approximation leads to roughly 10,000 DoF's less than the linear approximation.

So despite requiring a coarser mesh, the quadratic approximation yields similar results as those provided by the linear approximation, as attested by Figs. 21a and 21b, which show the horizontal and vertical velocity components $u_{h,1}$ and $u_{h,2}$ along the vertical line segment $x = 1$

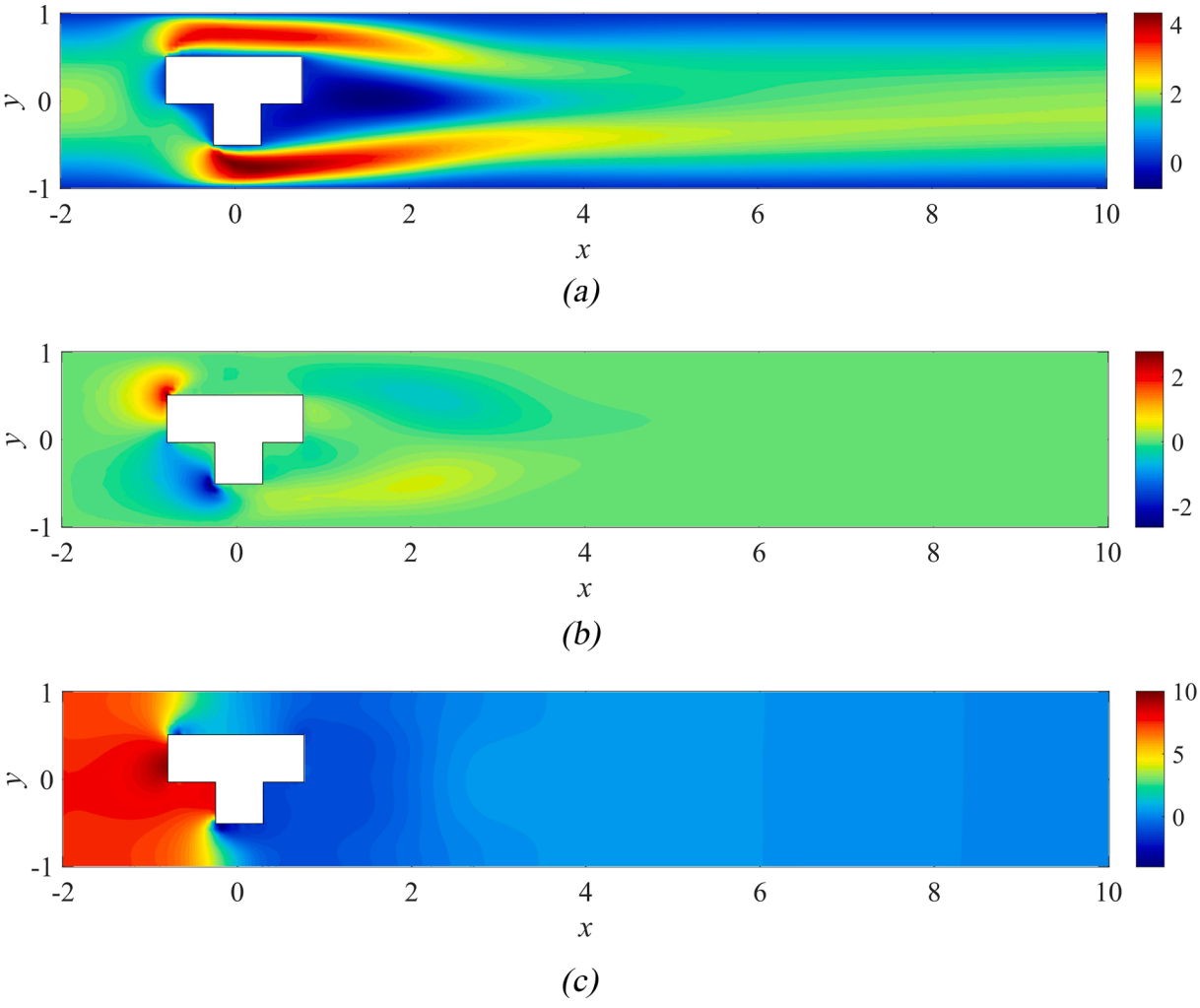

Fig. 20. The fields at $Re = 50$ provided by the $\mathbf{OFE}_1/\mathrm{OFE}_0$ pair. *(a)* The horizontal component of the velocity field $u_{h,1}$. *(b)* The vertical component $u_{h,2}$. *(c)* The pressure field p_h.

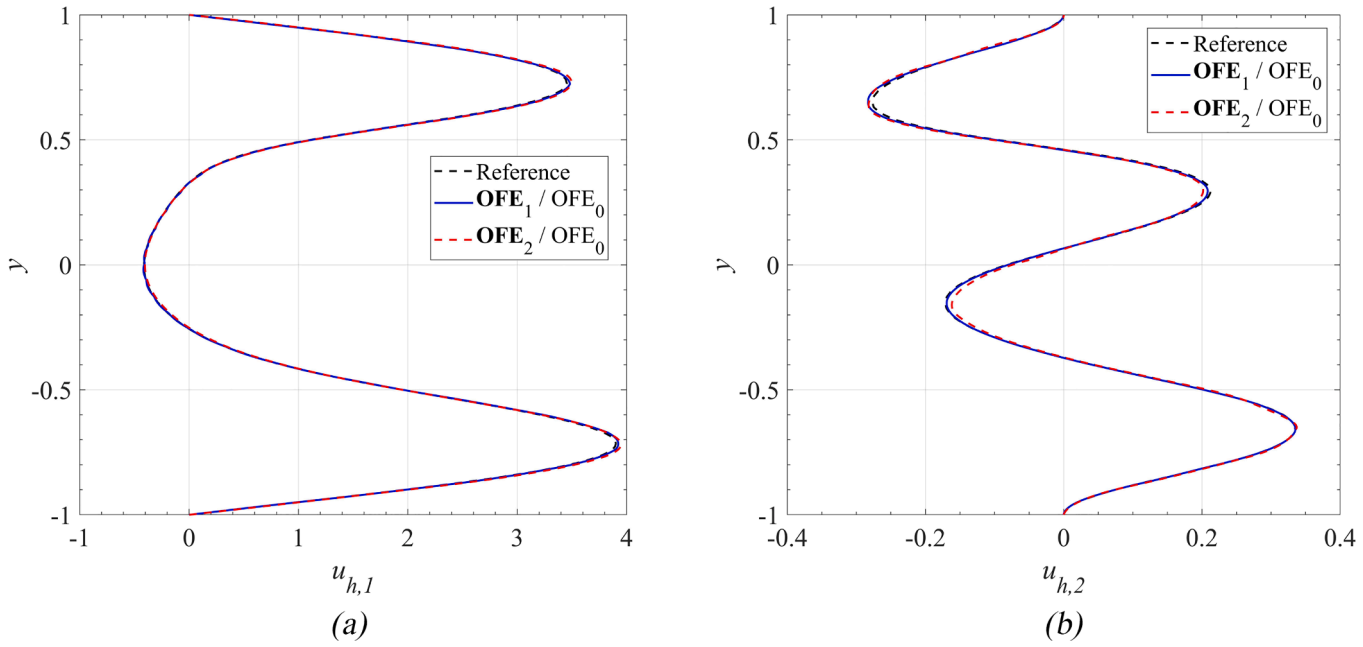

Fig. 21. Field profiles at $Re = 50$, provided by the $\mathbf{OFE}_1/\mathrm{OFE}_0$ and $\mathbf{OFE}_2/\mathrm{OFE}_0$ pairs, along the vertical line segment $x = 1$ and $-1 \leq y \leq 1$ (dotted orange line in Fig. 19a). *(a)* Horizontal component of the velocity field $u_{h,1}$. *(b)* Vertical component of the velocity field $u_{h,2}$. Reference solution given by the $\boldsymbol{Q}_2/Q_1$ pair, using the mesh of cells in Fig. 19b. (For interpretation of the references to colour in this figure legend, the reader is referred to the web version of this article.)

and $-1 \leq y \leq 1$, respectively.

These results demonstrate the ability of the $\mathbf{OFE}_2/\mathrm{OFE}_0$ pair to provide accurate solutions, even when coarse meshes are used. However, this pair is expensive, since it requires 6 DoF's per node for each component of the velocity. But as discussed previously in Section 4.3, in the AMORE paradigm the $\mathbf{OFE}_2/\mathrm{OFE}_0$ pair shall be used only at those few distorted elements close to boundaries and interfaces, which correspond roughly to 2% of the total number of elements in the mesh.

5. Concluding remarks

The focus of this paper was on the presentation of a parameter-free two-field mixed formulation for the solution of Navier-Stokes problems with inf-sup stable pairs of finite elements. The velocity field and the pressure are approximated by low-order quadrilateral overlapping finite elements (OFE), a family of general-purpose elements recently introduced for the solution of problems in solid mechanics [6]. In this paper we extended the OFE method to the study of fluid flows using only OFE in the mesh and also briefly discussed the important case of using traditional finite elements or control volume elements for fluid flows, coupling elements and overlapping elements, like used in AMORE [6].

We presented some theoretical aspects concerning the inf-sup stability and the well-posedness of the two-field mixed formulation, and verified that three pairs of velocity and pressure approximations satisfy the inf-sup condition using the Chapelle-Bathe numerical test. These pairs of velocity and pressure approximations could also directly be used to solve incompressible solid media by simply using displacements instead of velocities as unknowns.

Considering future investigations, other overlapping finite elements could be used in the discretization of the velocity and pressure fields, in particular for three-dimensional solutions. The idea is to use the tetrahedral, brick, prism, and pyramid elements proposed in [36,37] in the approximation of the velocity and introduce pressure fields. Then we must determine which pairs composed of these elements satisfy the inf-sup condition. The research work should also investigate the solution of flows at high Reynolds numbers [2,7,8,10,34], fluid flows with heat transfer [24], and fluid flows in general multiphysics applications [13,30].

An important additional research area is to study the AMORE scheme with the flexibility to use regular elements and OFE described by different nodal bases, that is, low- and high-order bases. A high-order basis might be used sparingly and only when the elements are very distorted. Indeed, it is a strength of using the OFE not having to change the mesh in an adaptive solution in order to reach a higher accuracy. Using this approach with a suitable error measure, combined with the generality and efficiency in the assemblage and solution of the governing equations, could lead to a very effective overall solution scheme in the analyses of solids, fluids and multiphysics.

Funding

This research did not receive any specific grant from funding agencies in the public, commercial, or not-for-profit sectors.

CRediT authorship contribution statement

Williams L. Nicomedes: Writing – review & editing, Writing – original draft, Visualization, Validation, Software, Methodology, Investigation, Formal analysis, Conceptualization. **Klaus-Jürgen Bathe:** Writing – review & editing, Validation, Supervision, Methodology, Investigation, Formal analysis, Conceptualization. **Fernando J.S. Moreira:** Supervision, Resources, Project administration. **Renato C. Mesquita:** Resources, Project administration.

Declaration of competing interest

The authors declare that they have no known competing financial interests or personal relationships that could have appeared to influence the work reported in this paper.

Data availability

Data will be made available on request.

References

[1] Atluri SN. The Meshless Method (MLPG) for Domain and BIE Discretizations. Tech Science Press; 2004.
[2] Banijamali B, Bathe KJ. The CIP method embedded in finite element discretizations of incompressible fluid flows. International Journal for Numerical Methods in Engineering 2007;71:66–80.
[3] Bathe K.J., Finite Element Procedures, Prentice Hall, 1996; 2nd ed. K.J. Bathe, Watertown, MA, 2014; and Higher Education Press, China, 2016.
[4] Bathe KJ. The inf-sup condition and its evaluation for mixed finite element methods. Computers and Structures 2001;79:243–52.
[5] Bathe K.J. The Finite Element Method with 'Overlapping Finite Elements', Proceedings of the Sixth International Conference on Structural Engineering, Mechanics and Computation – SEMC 2016, Cape Town, South Africa (A. Zingoni, ed.), 2016.
[6] Bathe KJ. The AMORE paradigm for finite element analysis. Advances in Engineering Software 2019;130:1–13.
[7] Bathe KJ, Zhang H. A Flow-Condition-Based Interpolation Finite Element Procedure for Incompressible Fluid Flows. Computers and Structures 2002;80:1267–77.
[8] Bathe KJ, Zhang H. Finite Element Developments for General Fluid Flows with Structural Interactions. International Journal for Numerical Methods in Engineering 2004;60:213–32.
[9] Bathe KJ, Zhang L. The finite element method with overlapping elements – A new paradigm for CAD driven simulations. Computers and Structures 2017;182:526–39.
[10] Bathe KJ, Pontaza JP. A flow-condition-based interpolation mixed finite element procedure for higher Reynolds number fluid flows. Mathematical Models and Methods in Applied Sciences 2002;12:525–39.
[11] Bathe KJ, Hendriana D, Brezzi F, Sangalli G. Inf-sup testing of upwind methods. International Journal for Numerical Methods in Engineering 2000;48:745–60.
[12] Bathe KJ, Iosilevich A, Chapelle D. An inf-sup test for shell finite elements. Computers and Structures 2000;75:439–56.
[13] Bathe KJ, Zhang H, Yan Y. The Solution of Maxwell's Equations in Multiphysics. Computers and Structures 2014;132:99–112.
[14] Brezzi F, Fortin M. Mixed and Hybrid Finite Elements. In: Springer Series in Computational Mathematics. Springer; 1991.
[15] Chai Y, Bathe KJ. Transient wave propagation in inhomogeneous media with enriched overlapping triangular elements. Computers and Structures 2020;237:1–20.
[16] Chapelle D, Bathe KJ. The inf-sup test. Computers and Structures 1993;47:537–45.
[17] Dautray R., Lions J.L. Mathematical Analysis and Numerical Methods for Science and Technology, Volume 6: Evolution Problems II. Springer; 2000.
[18] De S, Bathe KJ. Displacement/pressure mixed interpolation in the method of finite spheres. International Journal for Numerical Methods in Engineering 2001;51:275–92.
[19] De Loera J.A., Rambau J., Santos F. Triangulations: Structures for Algorithms and Applications, Springer Algorithms and Computation in Mathematics Series, Springer, 2010.
[20] Ern A, Guermond JL. Finite Elements II – Galerkin Approximation, Elliptic and Mixed PDEs, Springer Texts in Applied Mathematics. Springer; 2021.
[21] Ferrer E, Willden RHJ. A high order Discontinuous Galerkin Finite Element solver for the incompressible Navier-Stokes equations. Computers and Fluids 2011;46:224–30.
[22] Girault V, Raviart PA. Finite Element Methods for Navier-Stokes Equations: Theory and Algorithms. In: Springer Series in Computational Mathematics. Springer; 2011.
[23] Glowinski R., Finite element methods for incompressible viscous flow, Handbook of Numerical Analysis, Volume 9: Numerical Methods for Fluids (Part 3), P. G. Ciarlet and J. L. Lions, Editors, North-Holland, 2003.
[24] Guo Y, Bathe KJ. A numerical study of a natural convection flow in a cavity. International Journal for Numerical Methods in Fluids 2002;40:1045–57.
[25] Ham S, Lai B, Bathe KJ. The method of finite spheres for wave propagation problems. Computers and Structures 2014;142:1–14.
[26] Hjelle O, Daelen M. Triangulations and Applications, Springer Mathematics and Visualization Series. Springer; 2006.
[27] Huang J, Bathe KJ. Quadrilateral overlapping elements and their use in the AMORE paradigm. Computers and Structures 2019;222:25–35.
[28] Huang J, Bathe KJ. Overlapping finite element meshes in AMORE. Advances in Engineering Software 2020;144:1–13.
[29] Huang J, Bathe KJ. On the convergence of overlapping elements and overlapping meshes. Computers and Structures 2021;244:1–11.
[30] Jin D, Ledger PD, Gil AJ. *hp*-Finite element solution of coupled stationary magnetohydrodynamics problems including magnetostrictive effects. Computers and Structures 2016;164:161–80.
[31] Kim KT, Bathe KJ. Transient implicit wave propagation dynamics with the method of finite spheres. Computers and Structures 2016;173:50–60.
[32] Kim KT, Zhang L, Bathe KJ. Transient implicit wave propagation dynamics with overlapping finite elements. Computers and Structures 2018;199:18–33.
[33] Ko Y, Bathe KJ. Inf-sup testing of some three-dimensional low-order finite elements for the analysis of solids. Computers and Structures 2018;209:1–13.
[34] Kohno H, Bathe KJ. A flow-condition-based interpolation finite element procedure for triangular grids. International Journal for Numerical Methods in Fluids 2006;51:673–99.
[35] Lai B, Bathe KJ. The method of finite spheres in three-dimensional linear static analysis. Computers and Structures 2016;173:161–73.
[36] Lee S, Bathe KJ. An enhancement of overlapping finite elements. Computers and Structures 2022;260:106704.
[37] Lee S, Bathe KJ. Additional overlapping finite elements – The pyramid and prism elements. Computers and Structures 2022;268:106813.
[38] Lee S, Bathe KJ. Solution of the generalized eigenvalue problem using overlapping finite elements. Advances in Engineering Software 2022;173:103241.
[39] Li BQ. Discontinuous Finite Elements in Fluid Dynamics and Heat Transfer. Springer Computational Fluid and Solid Mechanics Series: Springer-Verlag; 2006.
[40] Liu GR. Meshfree Methods: Moving Beyond the Finite Element Method. 2nd Edition. CRC Press; 2010.
[41] Najafi M, Dehghan M, Sarler B, Kosec G, Mavric B. Divergence-free meshless local Petrov-Galerkin method for Stokes flow. Engineering with Computers 2022;38:5359–77.
[42] Nicomedes WL, Mesquita RC, Moreira FJS. Calculating the band structure of photonic crystals through the meshless local Petrov-Galerkin (MLPG) method and periodic shape functions. IEEE Transactions on Magnetics 2012;48:551–4.
[43] Nicomedes WL, Mesquita RC, Moreira FJS. The meshless local Petrov-Galerkin method in two-dimensional electromagnetic wave analysis. IEEE Transactions on Antennas and Propagation 2012;60:1957–68.
[44] Nicomedes WL, Bathe KJ, Moreira FJS, Mesquita RC. Meshfree analysis of electromagnetic wave scattering from conducting targets: Formulation and computations. Computers and Structures 2017;184:36–52.
[45] Nicomedes WL, Bathe KJ, Moreira FJS, Mesquita RC. The Method of finite spheres in acoustic wave propagation through nonhomogeneous media: Inf-sup stability conditions. *Vietnam Journal of Mechanics*, VAST 2020;42:209–37.
[46] Nicomedes WL, Bathe KJ, Moreira FJS, Mesquita RC. Acoustic scattering in nonhomogeneous media and the problem of discontinuous gradients: Analysis and inf-sup stability in the method of finite spheres. International Journal for Numerical Methods in Engineering 2021;122:3141–70.
[47] Rhebergen S, Wells GN. A Hybridizable Discontinuous Galerkin Method for the Navier–Stokes Equations with Pointwise Divergence-Free Velocity Field. Journal of Scientific Computing 2018;76:1484–501.
[48] Zhang L, Bathe KJ. Overlapping finite elements for a new paradigm of solution. Computers and Structures 2017;187:64–76.
[49] Zhang L, Kim KT, Bathe KJ. The new paradigm of finite element solutions with overlapping elements in CAD – Computational efficiency of the procedure. Computers and Structures 2018;199:1–17.
[50] Zienkiewicz OC, Taylor RL, Nithiarasu P. The Finite Element Method for Fluid Dynamics. 7th Edition. Butterworth-Heinemann; 2013.